Caveolae in the CNS arterioles mediate neurovascular coupling

Brian W. Chow[1], **Vicente Nuñez**[1], **Luke Kaplan**[1], **Adam J. Granger**[1,2], **Karina Bistrong**[1], **Hannah L. Zucker**[1], **Payal Kumar**[1], **Bernardo L. Sabatini**[1,2], **Chenghua Gu**[1]

[1]Department of Neurobiology, Harvard Medical School, 220 Longwood Ave, Boston, MA 02115, USA.

[2]Howard Hughes Medical Institute, Department of Neurobiology, Harvard Medical School, 220 Longwood Ave, Boston, MA 02115, USA.

Summary

Proper brain function depends on neurovascular coupling: neural activity rapidly increases local blood flow to meet moment-to-moment changes in regional brain energy demand[1]. Neurovascular coupling is the basis for functional brain imaging[2], and its impairment is implicated in neurodegeneration[1]. The underlying molecular and cellular mechanisms of neurovascular coupling remain poorly understood. The conventional view is that neurons or astrocytes release vasodilatory factors that act directly on smooth muscle cells (SMC) to induce arterial dilation and increase local blood flow[1]. Here, using two-photon microscopy to image neural activity and vascular dynamics simultaneously in the barrel cortex of awake mice under whisker stimulation, we found that arteriolar endothelial cells (aECs) play an active role in mediating neurovascular coupling. We found that aECs, unlike other vascular segments of ECs in the CNS, have abundant caveolae. Acute genetic perturbations that eliminated caveolae in aECs, but not in neighboring SMCs, impaired neurovascular coupling. Strikingly, caveolae function in aECs is independent of the eNOS-mediated nitric oxide (NO) pathway. Ablation of both caveolae and eNOS completely abolished neurovascular coupling, whereas each single mutant exhibited partial impairment, revealing that caveolae-mediated pathway in aECs is a major contributor to neurovascular coupling. Our findings indicate that vasodilation is largely due to ECs that actively relay signals from the CNS to SMCs via a caveolae-dependent pathway.

Despite representing only 2% of body mass, the brain uses 20% of the body's energy at rest and has very limited ability to store energy[3]. To meet moment-to-moment changes in regional brain energy demand, neural activity rapidly increases local blood flow, a process called neurovascular coupling[1]. Neurovascular coupling is also the basis for functional brain

---

Correspondence: Chenghua Gu (chenghua_gu@hms.harvard.edu), Department of Neurobiology, Harvard Medical School, Boston, MA 02115, U.S.A., (Ph) 617-432-6364 (Fax) 617-432-1639.

Competing Interests:
The authors declare no competing financial interests.

imaging, one of the few techniques currently available to image and measure activity in the human brain in both health and disease[2]. Impaired neurovascular coupling also has been implicated in neurodegeneration[1,3]. Despite the importance of neurovascular coupling, the underlying molecular and cellular mechanisms are still unclear.

Neurovascular coupling begins with increased neural activity and ends with SMC relaxation that leads to arteriolar vasodilation and increased capillary blood flow[2,4]. This process occurs rapidly, on the order of hundreds of milliseconds *in vivo* under physiological conditions[5–7]. How signals are transmitted from neurons to SMCs is not completely understood. The conventional view has been that following neural activity, neurons and astrocytes release vasodilatory signals that act directly on SMCs to relax and expand arteriolar diameter to increase blood flow[1]. However, recent studies have indicated that blood vessels can also sense neural activity changes[6,8,9], but the mechanisms underlying how these CNS endothelial cells (ECs) mediate neurovascular coupling remains largely unknown.

Here, we demonstrate that CNS aECs actively mediate signals from neurons to facilitate the relaxation of SMC during neurovascular coupling. We found that unlike other segments of ECs in the CNS vasculature, aECs have abundant caveolae. We used *in vivo* two-photon microscopy for simultaneous measurement of neural activity and vascular dynamics (arteriolar vessel diameter and capillary blood flow) in the barrel cortex of awake mice following whisker stimulation. We found that acute genetic perturbations that eliminated caveolae in aECs, but not in neighboring SMCs, impaired neurovascular coupling. Moreover, caveolae function in aECs is independent of the eNOS-mediated NO pathway, and ablation of both caveolae and eNOS completely abolished neurovascular coupling, revealing that the caveolae-mediated pathway in aECs is a major contributor to neurovascular coupling. Finally, we demonstrate that Mfsd2a, a molecular suppressor of caveolae formation, is absent in aECs and that ectopic expression of Mfsd2a specifically in aECs is sufficient to impair neurovascular coupling. Our findings indicate that vasodilation is due in large part to ECs that actively mediate signals from neurons and astrocytes to SMCs via a caveolae-dependent pathway.

CNS arteriolar endothelial cells have abundant caveolae

Previously, we discovered that caveolae are actively suppressed in most CNS ECs to ensure blood brain barrier integrity[10–12]. However, this suppression of caveolae is not uniform in all segments of the CNS endothelium since aECs have abundant caveolae (Fig. 1b,d), in contrast to negligible numbers of caveolae in capillary endothelial cells (cECs) (Fig. 1a,d). cECs and aECs can be distinguished under transmission election microscopy (EM) by the fact that capillaries have a smooth lumen whereas arterioles have a ruffled lumen, and cECs are enwrapped by pericytes, whereas aECs are ensheathed by SMCs (Fig. 1a,b). We demonstrate that these abundant vesicles in aECs are caveolae because these vesicles are abolished in aECs in *caveolin-1* mutant mice *(Cav1⁻/⁻)* (Fig. 1c,e). Cav1 is an obligatory component of caveolae, and *Cav1⁻/⁻* mice lack caveolae in the endothelium[11–14]. Thus, CNS aECs have abundant caveolae, a finding consistent with a previous study[15]. Interestingly, many caveolae are also present in SMCs that wrap the aECs (Fig. 1c,f).

Caveolae are essential for neurovascular coupling

Because caveolae are specifically abundant in aECs and CNS arterioles are the site of vasodilation[2,4], we examined *Cav1*$^{-/-}$ mice to determine whether caveolae are important for neurovascular coupling. To study neurovascular coupling *in vivo*, we optimized a two-photon microscope for simultaneous measurement of neural activity and vascular dynamics, including arteriolar vessel diameter and capillary blood flow, at single-vessel resolution in awake mice (Extended Data Fig. 1). We focused on the barrel cortex, a well-characterized region of mouse somatosensory cortex that processes sensory input from the vibrissae[16]. Sensory stimulation via whisker brushing in awake mice evoked spatially and temporally patterned neural activity that can be imaged in the barrel cortex by intracellular calcium levels in mice expressing the calcium sensor GCaMP6 in neurons (*Thy1:*^{GCaMP6s}) (Extended Data Fig. 1b,c). Hydrazide[5] and quantum dots were injected intravenously into *Thy1:*^{GCaMP6s} mice to visualize arterioles and image capillary blood flow, respectively. Upon whisker brushing, we observed a robust increase in the GCaMP signal in neurons, followed by increased arteriolar dilation and red blood cell velocity (measured by tracking the movement of red blood cells, which are devoid of quantum dots and thus appear dark) (Extended Data Fig. 1b–g) and Supplementary Videos 1, 2 and 3). Finally, in contrast to the robust vasodilation observed in the barrel cortex, under our *in vivo* whisker stimulation paradigm, the retrosplenial cortex, a brain region not associated with processing whisking[17], exhibits very low level of vasodilation (Extended Data Fig. 1h,i). This result indicates that the changes in arterial vessel diameter are a result of the whisker stimulus-dependent neural activity and not systemic variables.

Cav1$^{-/-}$ mice exhibited attenuated arteriolar dilation upon whisker stimulation whereas arterioles from wildtype *Cav1*$^{+/+}$ and heterozygous *Cav1*$^{+/-}$ mice dilated robustly (Fig. 2a,c,e and Extended Data Fig. 3a,i and Supplementary Video 4). Moreover, this vasodilation defect was observed in both pial arteries and penetrating arterioles diving deep into the parenchyma in *Cav1*$^{-/-}$ mice compared with their wildtype littermates (Extended Data Fig. 2). Importantly, the baseline diameter and latency to dilate were similar across the three genotypes (Extended Data Fig. 3b,c,d). These results suggest that the absence of caveolae does not impair basal vessel tone and kinetics but specifically impairs the amplitude of sensory-evoked arteriolar dilation. Consistent with the attenuation of arteriolar vasodilation, capillary blood flow was also impaired in mutant *Cav1*$^{-/-}$ mice upon whisker stimulation compared to control mice (Fig. 2b,d,f and Supplementary Video 5), whereas baseline capillary velocity and kinetics were similar across genotypes (Extended Data Fig. 3e,f). Moreover, the attenuated arteriolar dilation and capillary blood flow in mutant *Cav1*$^{-/-}$ mice were not due to either the impairment in sensory-evoked neural activity, or alteration in blood pressure because control and mutant mice display similar GCaMP6s dynamics in neurons (Extended Data Fig. 3g,h) and similar systolic, diastolic and mean blood pressure (Extended Data Fig. 3j). The normal blood pressure observed in *Cav*$^{-/-}$ mutant mice is consistent with previous studies[18]. Thus, these results demonstrate that caveolae are essential for optimal neurovascular coupling.

Because SMCs control arteriolar dilation during neurovascular coupling[2,4], we next examined whether the attenuated neurovascular coupling in *Cav1*$^{-/-}$ mice is due to impaired

integrity and function of SMCs. To visualize SMC morphology and vessel coverage, we intravenously injected Hydrazide into control $Cav1^{+/+}$; $NG2$:$^{DsRed+}$ and mutant $Cav1^{-/-}$; $NG2$:$^{DsRed+}$ mice. NG2:DsRed is a reporter for SMCs, oligodendrocytes, and pericytes[16,19]. By quantifying of the number of DsRed+ cells on Hydrazide+ arterioles, we established that there is normal coverage and morphology of SMCs in $Cav1^{-/-}$ mice compared to wildtype (Extended Data Fig. 4a,b). Moreover, we found similar expression of various contractile proteins including SMA, Myh11, Tagln, and Desmin in SMCs in wildtype littermates and $Cav1^{-/-}$ mice (Extended Data Fig. 4c–g).

To examine whether ablation of caveolae affects the ability of SMCs to respond to contractile and vasodilatory signals, we imaged arteriolar diameter changes in acute brain slices under two-photon microscopy after delivery of contractile and vasodilatory pharmacological compounds. We found that SMCs in $Cav1^{-/-}$ mice displayed normal contraction compared to wildtype controls following administration of U46619, a thromboxane A2 receptor agonist (Extended Data Fig. 4h,i and Supplementary Videos 6,7). When DEA-NONOate, a NO donor, was subsequently applied to the same vessel, we observed a similar level of dilation as the wildtype controls (Extended Data Fig. 4h,j and Supplementary Videos 6,7). Finally, to examine whether the impaired neurovascular coupling in mutant $Cav1^{-/-}$ mice is due to the inability of SMCs to relax following release of vasodilatory signals *in vivo*, we used two-photon microscopy in anesthetized mice imaged changes in vasodilation upon superfusing DEA-NONOate onto the pia of control $Cav1^{+/+}$ and mutant $Cav1^{-/-}$ mice. Upon acute administration of DEA-NONOate, the SMCs from both control $Cav1^{+/+}$ and mutant $Cav1^{-/-}$ mice relax and dilate arterioles at similar levels *in vivo* (Extended Data Fig. 4k,l and Supplementary Videos 8,9). These experiments demonstrate that the absence of caveolae impairs neurovascular coupling despite the presence of functionally normal SMCs.

Caveolae are specifically required in aECs but not SMCs for normal neurovascular coupling

Caveolae are present in both CNS aECs and SMCs (Fig 1c,d). We next tested whether caveolae function in a cell-autonomous manner using acute, cell-type-specific deletion of $Cav1$ in adult mice. First, we crossed BMX:^{CreER} mice, a tamoxifen-inducible aEC-specific driver line[20], with $Cav1$ floxed mice ($Cav1^{fl/fl}$)[21] to acutely ablate caveolae only in aECs. After tamoxifen treatment, Cav1 was specifically lost in aECs but not in SMCs of BMX:$^{CreER+}$;$Cav1^{-/fl}$ mutant mice with Cav1 protein present in both aECs and SMCs in BMX:$^{CreER-}$;$Cav1^{+/fl}$ control mice. (Extended Data Fig. 5a,c). EM analysis showed that in the barrel cortex of mutant BMX:$^{CreER+}$;$Cav1^{-/fl}$ mice, caveolae were ablated acutely in aECs but still present in SMCs, whereas abundant caveolae were present in both CNS aECs and SMCs in control BMX:$^{CreER-}$;$Cav1^{+/fl}$ mice (Extended Data Fig. 5b,d). Using our *in vivo* imaging paradigm, we found attenuation in arteriolar dilation (Fig. 2g,i and Extended Data Fig. 6a) and capillary blood flow (Fig. 2h,j) in BMX:$^{CreER+}$;$Cav1^{-/fl}$ mutant mice upon whisker stimulation, similar to what was observed in the $Cav1^{-/-}$ mutant mice (Fig. 2a–f). Baseline and kinetics of arteriolar diameter and capillary blood flow were unaffected in tamoxifen-treated BMX:$^{CreER+}$;$Cav1^{-/fl}$ mutant mice (Extended Data Fig. 5e,f and Extended

Data Fig. 6b–d). Together, these experiments demonstrate caveolae in aECs are important for neurovascular coupling.

To test the role of SMC caveolae in neurovascular coupling, we crossed *Myh11:CreER+* mice, a tamoxifen-inducible SMC driver line[22], to *Cav1* floxed mice to acutely ablate caveolae in SMCs. After tamoxifen treatment, we found that both Cav1 protein and caveolae were ablated successfully in SMCs but preserved in aECs in *Myh11:CreER+;Cav1−/fl* mutant mice (Extended Data Fig. 7a–d). However, in contrast to the attenuated neurovascular coupling observed in mice lacking Cav1 in aECs, no changes in arteriolar dilation and capillary blood flow after whisker stimulation were observed in mutants lacking Cav1 and caveolae in SMCs (Extended Data Fig. 6e–h and Extended Data Fig. 7e–j). This result indicates that caveolae in SMCs play little to negligible role in neurovascular coupling.

Caveolae in aECs mediate neurovascular coupling independently of eNOS

Next, we examined how aECs utilize caveolae to mediate neurovascular coupling. Caveolae have been implicated in many cellular processes[23], including transcytosis[11,12], serving as a membrane reservoir during mechanical stretch[24], clustering receptors and ion channels[25], and mediating intracellular signaling[26]. We focused on NO signaling because NO is a major vasodilatory factor in neurovascular coupling[27] and previous studies have reported that Cav1 interacts physically with endothelial NO synthase (eNOS/*nos3*)[28]. We first examined whether eNOS and NO levels are altered in the absence of caveolae. Surprisingly, we found similar levels of eNOS protein and NO in aECs between wildtype control and *Cav1−/−* mice, whereas both eNOS protein and NO signal were absent in *eNOS−/−* mice (Extended Data Fig. 8a–d). To examine genetic interactions between *Cav1* and *eNOS*, we characterized neurovascular coupling in *Cav1−/−*; *eNOS−/−* double mutant mice. We reasoned that if Cav1 and eNOS are in the same genetic pathway, the double mutants should phenocopy one of the single knockout mice, whereas if they function in separate and parallel pathways, the double knockout should have an additive phenotype of the two single knockout mice. With our *in vivo* imaging paradigm, *eNOS−/−* mice displayed attenuated arteriolar dilation and capillary blood flow upon whisker stimulation (Fig. 3a–d) consistent with a previous report[27]. Strikingly, the *Cav1−/−*; *eNOS−/−* double mutant mice completely lost arteriolar dilation and red blood cell velocity enhancement upon whisker stimulation, compared to a partial reduction in *Cav1−/−* and *eNOS−/−* single mutants (Fig. 3a–d and Extended Data Fig. 8e,f). These results demonstrate that caveolae-mediated neurovascular coupling is independent of the NO pathway. Moreover, the caveolae-mediated pathway is at least as important as the NO pathway for neurovascular coupling.

Ectopic expression of Mfsd2a in aEC downregulates caveolae and attenuates neurovascular coupling

We next asked why cECs have few caveolae whereas aECs have abundant caveolae. Previously, we discovered that Mfsd2a expression in CNS cECs actively suppressed caveolae formation and that this was necessary for blood-brain barrier integrity[10–12]. Using immunohistochemistry, we found that Mfsd2a protein was undetectable in aECs in both brain and retina (Fig. 4a,d and Extended Data Fig. 9a–d). Consistent with this result, Mfsd2a

transcript levels are also low in aECs compared to cECs[29]. Thus, CNS cECs robustly express Mfsd2a to suppress caveolae, whereas aECs lack Mfsd2a and are enriched in caveolae. We therefore examined whether ectopic expression of Mfsd2a specifically in CNS aECs is sufficient to suppress caveolae in aECs, and if so, our results so far predict that this suppression of caveolae in aECs would result in an attenuated neurovascular coupling.

To ectopically express Mfsd2a only in aECs, we generated a transgenic mouse where Mfsd2a expression is Cre-dependent (refered to as $R26^{:LSL-Mfsd2a}$, Extended Data Fig. 10a,b) and crossed it to $BMX^{:CreER+}$. After tamoxifen treatment, Mfsd2a protein was expressed abundantly in aECs in brains from $BMX^{:CreER+}$; $R26^{:LSL-Mfsd2a/+}$ mice, whereas control, $BMX^{:CreER-}$; $R26^{:LSL-Mfsd2a/+}$ adult mice lacked Mfsd2a expression in brain arterioles (Fig. 4b,e). Moreover, under EM, caveolae density was reduced significantly in $BMX^{:CreER+}$; $R26^{:LSL-Mfsd2a/+}$ mice relative to control (Fig. 4c,f). Strikingly, *in vivo* imaging revealed an attenuation of arteriolar dilation upon whisker stimulation in mice with Mfsd2a overexpression in aECs ($BMX^{:CreER+}$; $R26^{:LSL-Mfsd2a/+}$) relative to control mice ($BMX^{:CreER-}$; $R26^{:LSL-Mfsd2a/+}$) (Fig. 4g,h,i and Extended Data Fig. 10e). These experiments demonstrate that ectopic overexpression of Mfsd2a in CNS aECs is sufficient to reduce caveolae density and impair neurovascular coupling. Furthermore, inhibition of caveolae vesicles specifically in aECs using two different approaches, overexpression of Mfsd2a and genetic deletion of Cav1, both resulted in attenuated neurovascular coupling, demonstrating the importance of caveolae in CNS aECs for mediating neurovascular coupling.

Discussion

We used natural stimuli under physiological conditions in awake mice while simultaneously measuring neural activity and vascular dynamics under two-photon microscopy to study mechanisms underlying neurovascular coupling. We discovered that caveolae in CNS aECs are important to mediate neurovascular coupling. In addition, we confirmed that the previously reported eNOS pathway is also important for neurovascular coupling[27]. However, we found that the caveolae-mediated pathway is independent of eNOS signaling as the perturbation of both caveolae- and eNOS-mediated pathways together completely abolished neurovascular coupling, whereas ablation of each pathway alone results in partial impairment. Thus, these findings reveal that the caveolae-mediated pathway is at least as important as the NO pathway for neurovascular coupling.

Previous studies first highlighted the importance of ECs in neurovascular coupling *in vivo*. Locally disrupting ECs via optically-induced reactive oxygen species (ROS) halted propagation of stimulus-evoked vasodilation in pial arteries[6]. Here, our findings have extended this work to identify and demonstrate specific molecular and subcellular components in aECs that are essential for neurovascular coupling using cell-type specific genetic manipulations. Given the recent evidence that cECs are involved in sensing neural activity changes and are important for neurovascular coupling[2,6,8], we envision that after sensing nearby increased neural activity, cECs relay this signal electrically to the upstream aECs, which in turn send vasodilatory cues to SMCs via a caveolae-dependent process. How could caveolae carry out this function? Although caveolae have been reported to serve as a

membrane reservoir during mechanical stretch,[24] it is unlikely that the attenuated vasodilation observed in $Cav1^{-/-}$ mutant mice results from impaired arteriolar elasticity given that superfusing NO donor *in vivo*, which dilates arterioles by directly relaxing SMC, produced similar dilations in wildtype and mutant $Cav1^{-/-}$ mice (Extended Data Fig. 4k,l and Supplementary Videos 8,9). Similarly, previously described interactions between caveolae and the eNOS signaling pathway cannot explain the impaired vasodilation observed in $Cav1^{-/-}$ mutant mice because simultaneous ablation of both caveolae- and eNOS-mediated pathways abolishes neurovascular coupling, whereas ablation of either pathway alone results in partial impairment. In light of these results, caveolae's ability to cluster ion channels and receptors[30], several of which have been implicated in vasodilation[8], most likely explains its role in neurovascular coupling. In aECs, caveolae could cluster these channels to facilitate transmission of vasodilatory signals to SMCs. Identifying the channels that clustered within caveolae in aECs will be an important next step to address for the field.

Our results also demonstrate that CNS ECs from different vascular segments exhibit heterogeneity at molecular, cellular, and functional levels. Here we show that this endothelial heterogeneity governs the two unique and important functions of the CNS vasculature: the blood-brain barrier and neurovascular coupling. We found cECs express Mfsd2a, which suppresses caveolae to ensure blood-brain barrier integrity[10–12]. In contrast, aECs lack Mfsd2a and concurrently have abundant caveolae, which are important for neurovascular coupling. We expect this kind of heterogeneity to exist broadly in CNS ECs and that understanding this heterogeneity will advance our understanding of the diverse functions of ECs in health and disease. Given that neurovascular coupling is impaired in various neurological disorders[1], future studies examining whether these different molecular and cellular pathways are altered in disease may provide insight for development of novel therapies.

Methods

Animals

All animal experiments were approved by the Harvard University Institutional Animal Care and Use Committee (IACUC). The following mice strains were used: wildtype (C57BL/6J, Jackson Laboratory # 000664), *Mfsd2a:CreER*[31], *BMX:CreER*[20], *Myh11:CreER*[22], *NG2:DsRED*[19] JAX# 008241, *Ai14*[32] JAX# 007914, *Ai39*[33] JAX# 014539, *Ai75*[34] JAX# 014539, *ROSA26:LSL-Mfsd2a* (this study), *Thy1:GCaMP6s*[35] JAX# 024275, *Cav1*[−/−][13] JAX# 007083, *Cav1* floxed[21], *Nos3*[−/−][36] JAX# 002684, ROSA26: PhiC31[37] JAX# 007743. All mice were maintained on a mixed background and both males and females were used. For adult mice expressing *CreER*, tamoxifen (Sigma-Aldrich, T5648) was dissolved in corn oil at a concentration of 20 mg/ml and injected into peritoneal cavities with 0.2 mg/g body weight. Six-week-old to seven-week-old mice were treated with tamoxifen for five consecutive days and were allowed to recover for one week following the last tamoxifen treatment. Afterward, cranial surgery or dissections were performed. Randomization was determined by mouse genetics as wildtypes, mutants and transgenic were assigned randomly into their respective genotype group. Sample sizes were determined by a power calculation

based on previous pilot data and representative sample sizes from previous literature that had similar experiments.

Generation of *ROSA26:LSL-Mfsd2a* transgenic mice

The targeting vector contains a CAG promoter and loxP-3xSV40PA-loxP followed by mMfsd2a cDNA and WPRE-PolyA. A positive selection cassette, attB-PGKNeoR-attP, is located between the insertion and the 3' homologous arm which is 4.3 kb. The length of the 5' homologous arm is 1.1 kb (Please see Extended Data Fig. 10).

The targeting vector was electroporated into ES cells derived from F1 hybrid blastocyst of 129S6 x C57BL/6J. The G418 resistant ES clones were screened by nested PCR using primers outside the construct paired with primers inside the insertion cassette. The positive ES cell clones were used to generate chimeric mice by aggregating with 8-cell embryos of CD-1 strain. The attB-Neo-attP cassette was removed in mice by crossing the chimeras with R26PhiC31 females (JAX# 007743) backcrossed in C57BL/6J for 13 generations. The F1 pups were genotyped by PCR using primers set (5'- CCAAAGTCGCTCTGAGTTGT –3'); (5'- CCAGGTTAGCCTTTAAGCCT –3') and (5'- CGGGCCATTTACCGTAAGTT-3'). The PCR products are 250 bp for the wildtype allele and 329 bp for the mutant allele.

Long-term Cranial Window Surgery

Six-week-old to four-month-old mice underwent a craniotomy, implantation of a sterile glass window (3.0 mm) and attachment of a customized titanium head plate to the skull using dental cement (Metabond Parkell Inc.). Prior to the craniotomy, an intramuscular dose of Dexamethasone (120 mg/kg) was administered. Mice were anesthetized with 3–5% Isoflurane and maintained at 1–2% Isoflurane for the duration of the craniotomy. The respiration rate and body temperature were continuously monitored throughout the procedure to ensure the appropriate level of anesthesia. A subcutaneous dose of the analgesic: Buprenorphine (0.1 mg/kg) and Ketoprofen (5.0 mg/kg) was administered at the onset of the procedure and was also administered daily for two additional days after the craniotomy. A single dose of the local anesthetic Lidocaine (20 mg/kg) / Bupivacaine (2.5 mg/kg) was administered subcutaneously at the site the craniotomy. The center of the craniotomy over the barrel cortex and retrosplenial cortex were determined for each mouse in relation to the skull indentations bregma and lambda. Generally, for barrel cortex surgery, 3.5 – 3.8 mm posterior and 1.5 mm laterally from the midpoint between bregma and lambda along the sagittal suture was marked as the center of the craniotomy. For retrosplenial cortex surgery, the center of the craniotomy was 3.2–3.5 mm posterior and 1.0 mm lateral from Bregma. Following the craniotomy and the window with head plate implantation, mice were treated with Buprenorphine/ Ketoprofen and observed for signs of pain and/or infection for 72 hours. Furthermore, mice were handled by the experimenter, habituated to head restraint and trained to run on a foam ball daily for three consecutive days. Sensory-evoked arteriolar dilation and capillary blood flow were imaged through a 3.0 mm diameter cranial window positioned over the somatosensory cortex in head-restrained mice with the freedom to walk on a bidirectional Styrofoam ball.

Two-photon microscopy

Two-photon imaging was performed using a custom-built microscope equipped with a tunable Ti:Sapphire laser (MaiTai HP DS, Spectra-Physics) controlled by ScanImage 5.1 (Vidrio Technologies). The intensity of the femtosecond pulsed infrared beam was controlled by an electro-optical modulator (Conoptics Inc.) and passed through a pair of scan mirrors (Cambridge Technology) that enabled image acquisition at 30 Hz for a field of view of 1.0 mm^2 and 512×512 pixels. Control of image zoom was enabled by controlling the resonant scanner amplitude. The objective lens used was a 16x, 0.8 NA, water immersion from Nikon. Green and red fluorescence photons were separated using a custom-sized dichroic beamsplitter (580 BrightLine®, Semrock) and two custom-sized single-band bandpass filters (525/50 nm BrightLine®, 641/75 nm BrightLine®, Semrock). Fluorescence photons were collected using photomultiplier tubes (Hamamatsu).

In vivo imaging of pial arteriolar dilation and analysis

Arterioles labeled with Alexa Fluor™ Hydrazide 633 were imaged at 800 nm with a field of view size of 200 μm x 200 μm (512×512 pixels, pixel size of 0.16 μm^2/pixel) at 30 Hz. Whisker stimulation (4 Hz, 5 s) was performed using a foam brush controlled by a servo motor under the control of WaveSurfer. Alexa Fluor™ 633 Hydrazide (5 mg/kg) was intravenously injected into mice to visualize arterioles *in vivo*[5]. We imaged surface-level pial arteries and arterioles from the middle cerebral artery. Our selection of arteries and arterioles were guided by Hydrazide+ vessels, which labels arteries and arterioles only[5,7]. Because we are stimulating the entire whisker pad (Extended Figure 1) as opposed to stimulating individual whiskers, we observed changes in all sampled branches. This is consistent with the findings from Hill *et al.* [16] that branch orders were not necessarily relevant as long as the vessels were arterial (which they defined as SMA+ or Hydrazide+). Three technical trials were acquired and averaged for each field of view. 10–13 fields of view were acquired per imaging session. Three imaging sessions were collected on three separate days per mouse and arteriolar dilation responses were averaged across all three sessions for each mouse. To determine percent change in diameter relative to baseline, the time series were first filtered with a Gaussian blur and background subtracted with a rolling ball of 50 pixels. Five line-scans orthogonal to the arterioles were sampled to generate kymographs. The two max intensity peaks (which represent the walls of the arterioles) were identified across the kymograph. The change in diameter of the arterioles was determined as (diameter$_{time}$ − diameter$_{baseline}$)/diameter$_{baseline}$. Diameter baseline was determined as the mean diameter during the 3 seconds prior to the whisker stimulation. The change in max diameter was determined as the max value during the whisker stimulation. To determine latency onset to dilate, a line was fitted through 80% and 20% of max value. The latency onset to dilate was considered the time difference between the x-intercept of the line and the start of the whisker stimulation.

In vivo imaging of parenchymal arteriolar dilation and analysis

Arterioles stained with Alexa Fluor™ 633 Hydrazide (5 mg/kg) were imaged at multiple depths within the barrel cortex. Three parenchymal depths were used at 100 μm, 200 μm and 300 μm from the pial surface. Three technical trials were acquired and averaged for each

field of view at each depth location. 3–4 diving arterioles were imaged per imaging session and three sessions on sequential days were recorded in total per mouse. For analysis of parenchymal arterial dilation which appear as ellipses, we tracked the diving arterioles by fitting an ellipse to the Hydrazide signal. Movies were first averaged using a three frame rolling average then smoothed with a Laplacian of Gaussian filter. Intensities of the smoothed movie were rescaled to range from 0 to 255 and a threshold pixel intensity was picked to exclude background fluorescence signal outside of the ring of Hydrazide signal surrounding the arteriole. Next, ridge detection was performed using the FIJI ridge detection plugin[38]. Three separate ridge detection parameter sets were used and the ridges were combined to detect bright and dim ridges. Next, an initial estimate of the ellipse fit was determined using an elliptical Hough transform on the binarized ridge image. The fit was then refined by minimizing the distance between the ridge pixels and the fitted ellipse using the Hough transform results as the starting parameter values. The ellipse was parameterized as follows:

$$x(\propto) = a * \cos(\propto)\cos(\theta) - b * \sin(\propto)\sin(\theta) + x\_o$$

$$y(\propto) = a * \cos(\propto)\sin(\theta) + b * \sin(\propto)\cos(\theta) + y\_o$$

Where $x(\alpha)$, $y(\alpha)$ are the x- and y- coordinates of the points on the ellipse, a and b are the two ellipse axes, θ is the tilt angle of the ellipse, x_o and y_o are the coordinates of the ellipse center, and α ranges from 0 to $2*\pi$ to circumscribe the entire ellipse perimeter. Minimization was done in MATLAB using the lsqnonlin function and 95% confidence intervals of the parameters were determined using nlparci. In order to be consistent with the pial artery dilation tracking, we report D/D from the minor axis of the ellipse, which does not depend on the orientation of the arteriole cross-section relative to the microscope optical axis. As image quality is variable, frames with poor accuracy fitting are discarded by first rejecting frames where the minor axis fit is more than two median absolute deviations from the 10-frame sliding window median. Next, frames that have a confidence interval greater than 4 pixels for the minor axis are discarded. If fewer than 50% of the frames of the trajectory remain, the entire trajectory is discarded. Finally, the trajectory was smoothed using the MATLAB smooth function with 'rlowess'. To obtain D/D, this value was multiplied by 2 and divided by the mean diameter immediately 3 seconds prior to whisker stimulation. The three technical were averaged as with the pial artery dilation experiments to produce the trajectory for the vessel.

In vivo imaging of capillary red blood cell velocity and analysis

Mice were intravenously injected with quantum dots 525 (Thermo Fisher Scientific) and Alexa Fluor™ Hydrazide 633 to unambiguously distinguish arterioles and capillaries *in vivo*. Hydrazide-negative capillaries were imaged with a field of view size of 100 μm x 25 μm (512×25 pixels, pixel size of 0.04 μm^2/pixel) at 610 Hz. Whisker stimulation (4 Hz, 5 s) was performed using a foam brush controlled by a servo motor under the control of Wavesurfer. Three technical trials were acquired and averaged for each field of view. Three imaging sessions were collected on three separate days per mouse and changes in capillary

red blood cell velocity were averaged across all three sessions for each mouse. To determine percent change in velocity relative to baseline, the movies were first filtered with a Gaussian blur and background subtracted with a rolling ball of 50 pixels. Five-line scans parallel to the flow of red blood cells were sampled to generate kymographs. Using a published algorithm[39] that uses a reiterative radon transform and edge detection filter, the change in velocity of red blood cells was determined as $(\text{velocity}_{time} - \text{velocity}_{baseline})/\text{velocity}_{baseline}$. Velocity baseline was defined as the mean velocity during the 3 seconds prior to the whisker stimulation. The change in max velocity was determined as the max value during the whisker stimulation. To determine latency onset to increase red blood cell velocity, a line was fitted through 80% and 20% of max velocity value. The latency onset was considered the time difference between the x-intercept of the fitted line and the start time of the whisker stimulation.

In vivo two photon imaging and pharmacology

To assess vasodilatory function of pial artery smooth muscle cells, we imaged pial artery diameter changes with two-photon microscopy in response to topical application of the nitric oxide donor DEA-NONOate (EMD Millipore). Arteries were stained with Alexa Fluor™ 633 Hydrazide, as described earlier, one day prior to the imaging session. Under Isoflurane anesthesia (1.0–1.5%), a titanium head-plate with a 10 mm diameter hole centered over the right parietal skull bone was cemented onto the skull using Metabond. A custom perfusion system was constructed along the rim of the head-plate hole to allow for simultaneous imaging and application of DEA-NONOate. A 5.0–7.0 mm circular craniotomy of the right parietal skull bone was carefully performed and the newly exposed cortex was kept submerged in artificial CSF for the duration of the experiment. The mouse was then carefully transitioned from Isoflurane (0.5%) to Ketamine/Xylazine (100 mg/kg) and transferred from the surgical stereotaxic stage to the imaging platform where body temperature was maintained at 37 °C using a heat pad. A fresh 1.0 μM DEA-NONOate solution was prepared immediately prior to the start of the imaging session given the short half-life of DEA-NONOate in aqueous solution. A syringe pump (Harvard Apparatus) controlled the application of the DEA-NONOate solution onto the exposed cortex at 1.0 ml/ min. Five recordings (30 s in duration) of each pial vessel per mouse where collected in series interleaved with 30 s of washing with artificial cerebral spinal fluid (aCSF). The five measurements were then averaged per mouse.

Ex vivo, acute slice two-photon slice imaging and pharmacology

Acute coronal brain slices were prepared by deeply anesthetizing mice with Isoflurane inhalation followed cardiac perfusion with ice-cold choline-based cut solution containing (in mM): 25 $NaHCO_3$, 25 Glucose, 1.25 NaH_2PO_4, 7 $MgCl_2$, 2.5 KCl, 0.5 $CaCl_2$, 11.6 ascorbic acid, 3.1 pyruvic acid, 110 Choline chloride. After brain dissection and blocking, 300 μm slices were prepared in cut solution with a Leica VT1000s vibratome. Slices were then transferred for 30 minutes to recovery into a holding chamber containing 34°C (aCSF) containing (in mM): 125 NaCl, 2.5 KCl, 1.25 NaH2PO4, 25 NaHCO3, 11 glucose, 2 CaCl2, 1 MgCl2. During recovery, slices were incubated with ~ 1 μM Alexa Fluor™™ 633 Hydrazide (ThermoFisher). Following recovery, slices were imaged while constantly perfused with room temperature aCSF. Choline cut solution and aCSF were constantly

bubbled with 5% CO2/95% O2. Imaging was performed on a custom-built 2-photon microscope and images acquired with a custom version of ScanImage written in MATLAB (Mathworks). During imaging, arteries were constricted with 100 nM U46619 (Sigma-Aldrich) and dilated by acutely dissolving ~ 5 mg of DEA-NONOate (EMD Millipore) into the 10 mL of recycling aCSF being perfused over the slice.

Non-invasive blood pressure measurement procedure in awake mice

Systolic, diastolic and mean blood pressure were measured using the non-invasive tail cuff method (CODA Monitor, Kent Scientific Corp). At the start of a blood pressure measurement session, the appropriate mouse holder was selected based on the mouse's weight. The holder was placed over a heating pad with a set temperature that is regulated at 38 °C. The tail-cuff and Volume Pressure Recording (VPR) sensor were placed on the heating pad and covered with a blanket to allow these components to reach the set temperature. After 2–3 minutes, the awake mouse was gently introduced into the holder. A light blanket was draped over the tail and the mouse was left alone for 3–5 minutes to allow habituation. The blood pressure measurements take place via 10–20 tail cuff inflation-deflation sweeps that in total take from 5–10 minutes in duration. Multiple days of measurements may be required to gain confidence in the accuracy of the measurements. After the measurements, the mouse was carefully removed from the holder and immediately placed in its cage. Measurements of all sweeps are then averaged per mouse.

Smooth muscle cell coverage quantification

NG2:DsRED (or *CSPG4:DsRED*) were crossed to *Cav1$^{-/-}$* mice. Cranial window surgeries were performed over the barrel cortex of *Cav1$^{+/+}$*; *NG2:^{DsRED}+* and *Cav1$^{-/-}$;NG2:^{DsRED}+* mice. Mice were injected with Alexa Fluor™ 488 Hydrazide (5 mg/kg). ~30 arterioles (Hydrazide+; DsRed+) per mice were imaged. A 100 μm intensity line profile was drawn perpendicularly to the contractile bands of the smooth muscle cells. Max peaks corresponding to individual smooth muscle were counted and the number of smooth muscle cells/100 μm length was determined.

Transmission electron microscopy

Brains from adult mice were dissected and fixed by immersion in 5% glutaraldehyde/4% PFA/0.1 M sodium-cacodylate for two weeks at room temperature. Following fixation, brains were washed overnight in 0.1 M sodium-cacodylate. Coronal vibratome free-floating sections of 50 μm were collected. The cortex, particularly somatosensory and motor, were micro-dissected, post-fixed in 1% osmium tetroxide and 1.5% potassium ferrocyanide, dehydrated, and embedded in epoxy resin. Ultrathin sections of 80 nm were then cut from the block surface, collected on copper grids, and counter-stained with Reynold's lead citrate and examined under a 1200EX electron microscope (JEOL) equipped with a 2k CCD digital camera (AMT).

Mean Vesicular Density

For all TEM quantifications, mean total vesicular density values were calculated from the number of vesicles per μm^2 of cell area for each image collected. All images were collected

at 12000x magnification and analysis was performed blinded. Each density value (circle on the graphs) represents an individual vessel (capillary or arteriole). The same color of the circle represents vessels analyzed from the same mouse. Values are expressed as mean ± s.e.m.

Immunohistochemistry

Mice with deeply anesthetized with ketamine/xylazine via intraperitoneal injection and then mice were transcardially perfused with cold PBS and followed by cold 4% PFA. Brains and retinas were fixed by immersion in 4% PFA/PBS overnight at 4 °C. Next, brains and retinas were washed 3x in PBS. Brain sections were either cut as 50 μm sections on the vibratome or cryopreserved in 30% sucrose, frozen in TissueTek OCT (Sakura) and cut as 25 μm sections on the cryostat. For Mfsd2a and eNOS immunohistochemistry, mice were sacrificed via cervical dislocation. Brains were snap-frozen with liquid nitrogen and cut as 25 μm sections on the cryostat. Brain sections were fixed with chilled methanol for 10 minutes. Brain sections and retinas were blocked with 10% goat or donkey serum/5% BSA/PBST (0.5% Triton X-100) and stained overnight at 4 °C with the following primary antibodies at the indicated concentrations: α-Mfsd2a (1:200, Cell Signaling Technologies; RRID: AB_2617168) or α-Mfsd2a (generous gift from Dr. David Silver as used previously[40], α-SMA (1:1000, Sigma-Aldrich Cat# C6198, RRID:AB_476856), α-ICAM2 (1:200, BD Biosciences Cat# 553326, RRID:AB_394784), α-PECAM (1:200, BD Biosciences #553370; RRID: AB_394816), α-Claudin-5 (Thermo Fisher Scientific Cat# 34–1600, RRID:AB_2533157), eNOS (Abcam Cat# ab5589, RRID:AB_304967), Myh11 (Abcam Cat# ab53219), RRID:AB_2147146), Desmin (Thermo Fisher Scientific Cat# PA1–37556) and Tagln (Abcam Cat# ab14106) followed by corresponding Alexa Fluor™-conjugated secondary antibodies (1:500, Thermo Fisher Scientific) and Alexa Fluor™ Hydrazide 633 (1:1000, Thermo Fisher Scientific). Tissues were mounted with ProLong Gold for imaging.

In situ NO detection

This assay was previously adapted from these studies[41,42]. Mice were deeply anesthetized with ketamine/xylazine. Mice were transcardially perfused with warm (37°C) 50 mL PBS, then perfused with 50 mL warm PBS containing 10 μM DAF-2 (Thermo Fisher Scientific, D23842), 100 μM L-Arginine and 2 mM $CaCl_2$. Next, mice were perfused with warm PBS again followed by 4% PFA. Brains and kidneys were harvested and fixed overnight in 4% PFA at 4°C. Tissues were sectioned on the vibratome (50 μm) and processed for immunostaining.

Light microscopy

Olympus FluoView FV1200 and Leica SP8 laser scanning confocal microscopes (20x, 0.75 N.A., 40x, 1.3 N.A., 63× 1.4 N.A.) and an Olympus VS 120 slide scanner (10x, 0.4 N.A.) were used for imaging retina flat-mounts and brain sections. Images were processed using Adobe Photoshop, Illustrator, Olympus Fluoview and FIJI (NIH).

Statistical analyses

All statistical analyses were performed using Prism 7 and 8 (GraphPad Software). Two group comparisons were analyzed using an unpaired two-tailed Student's t-test or non-parametric analyses. Multiple group comparisons were analyzed using a one-way ANOVA, followed by a post hoc Bonferroni analysis to correct for multiple comparisons. No data were excluded when performing statistical analysis. The standard error of the mean was calculated for all experiments and displayed as errors bars in graphs. Statistical details for specific experiments, including exact n values and what n represents, precision measures, statistical tests used, and definitions of significance can be found in Figure Legends. Each color circle on the graphs throughout the study represents an individual vessel (capillary or arteriole or smooth muscle cell). The same color of the circle represents vessels analyzed from the same mouse. Values are expressed as mean ± s.e.m. Please see Supplementary Table 1 for statistical test results.

Code Availability

The source code to run the pial arteriolar dilation analysis is available online: https://github.com/gulabneuro/Pial-Vasodilation-Analysis. The source code to run the parenchymal arterial dilation analysis is available online: https://github.com/gulabneuro/divingArterioleTracking

Data Availability

Source data for quantitation described in the text or shown in graphs plotted in Figures 1 –4 and Extended Data Figs. 1–10 are available.

Extended Data
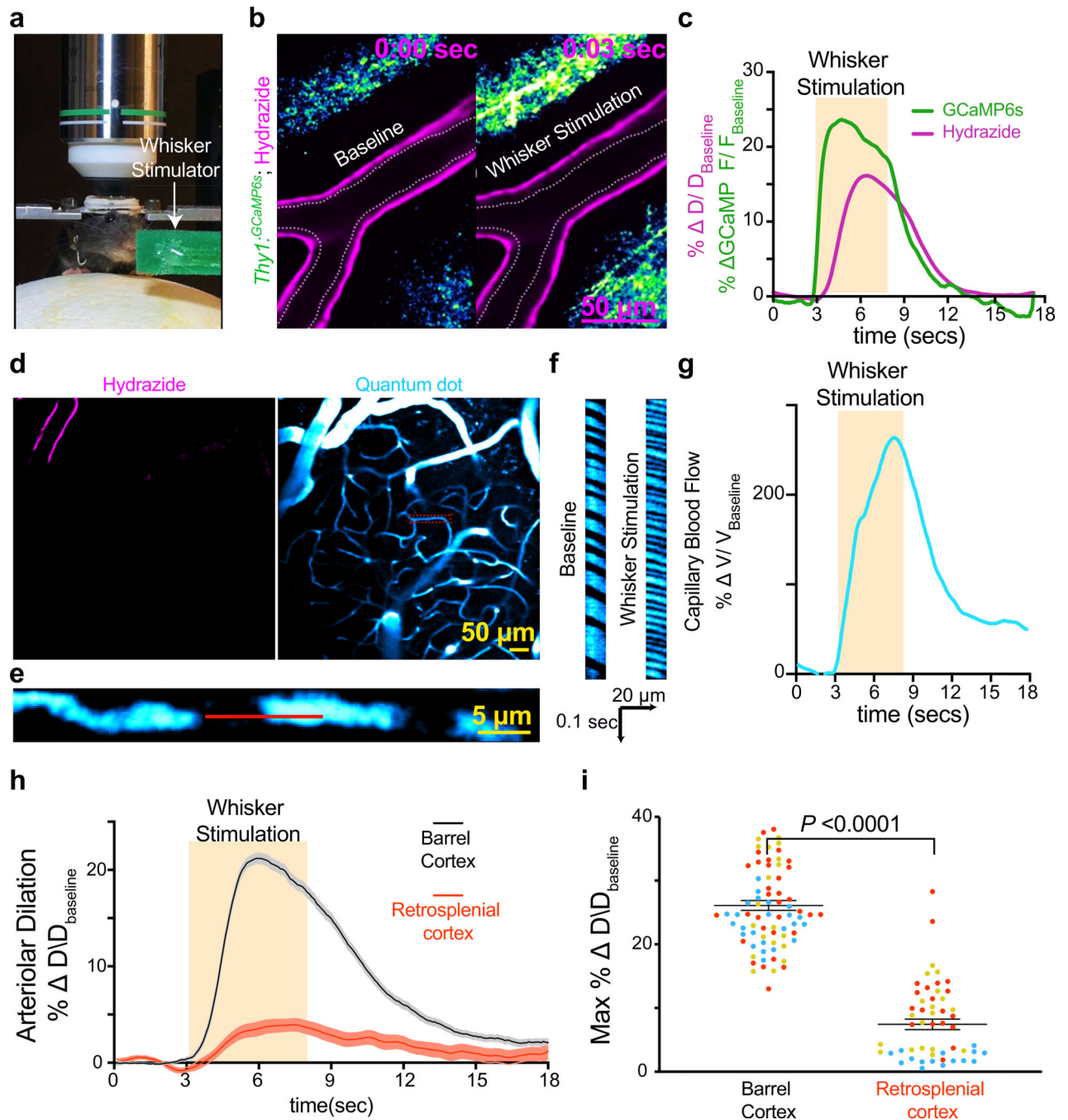
Extended Data Fig. 1. *In vivo* **two photon imaging of neurovascular coupling in the barrel cortex and retrosplenial cortex.**

a, Setup of the *in vivo* microscopy. Awake mice with cranial windows over the barrel cortex are head-fixed and allowed to move on a foam ball. Whisker stimulator (arrow) is used for brushing whiskers to evoke neural activity in the barrel cortex. (**b-g**) Imaging in the barrel cortex. **b,** Hydrazide injection in *Thy1:GCaMP6s* mice allows for simultaneous imaging of neural activity (green) and arteriolar dilation (magenta). Two-photon imaging of arterioles and neural activity before (left) and after (right) whisker stimulation. Hashes indicate the

baseline diameter at time = 0 sec. **c,** Time-course of change in arteriolar dilation (magenta) and GCaMP6s fluorescence (green). Orange bar signifies the period of whisker stimulation. **d**, Two-photon imaging of arterioles (magenta) and capillary blood flow (blue). After intravenous injection of quantum dots, the plasma is bright whereas the red blood cells are dark. **e,** High magnification of a capillary outlined by the red box in (**d**). Minimizing the image size increases the temporal resolution to ~610 Hz or 1.6 msec per frame. **f,** Kymographs of capillary blood flow during baseline (left) and whisker stimulation (right). Kymographs were generated from the parallel line scan (red line) of the capillary blood flow in (**e**). **g,** Time-course of change in red blood cell velocity. **h.** Time-course of change in arteriolar dilation in the barrel cortex (black, n= 78 arterioles; 3 mice) and in the retrosplenial cortex (red, n=54, 3 mice). (**i**) max % change in arteriolar dilation upon whisker stimulus in these two brain regions upon whisker stimulus. The orange bar signifies the period of whisker stimulation. All data is mean ± s.e.m. Statistical significance was determined by a nested unpaired, two-tailed t-test for (**i**).
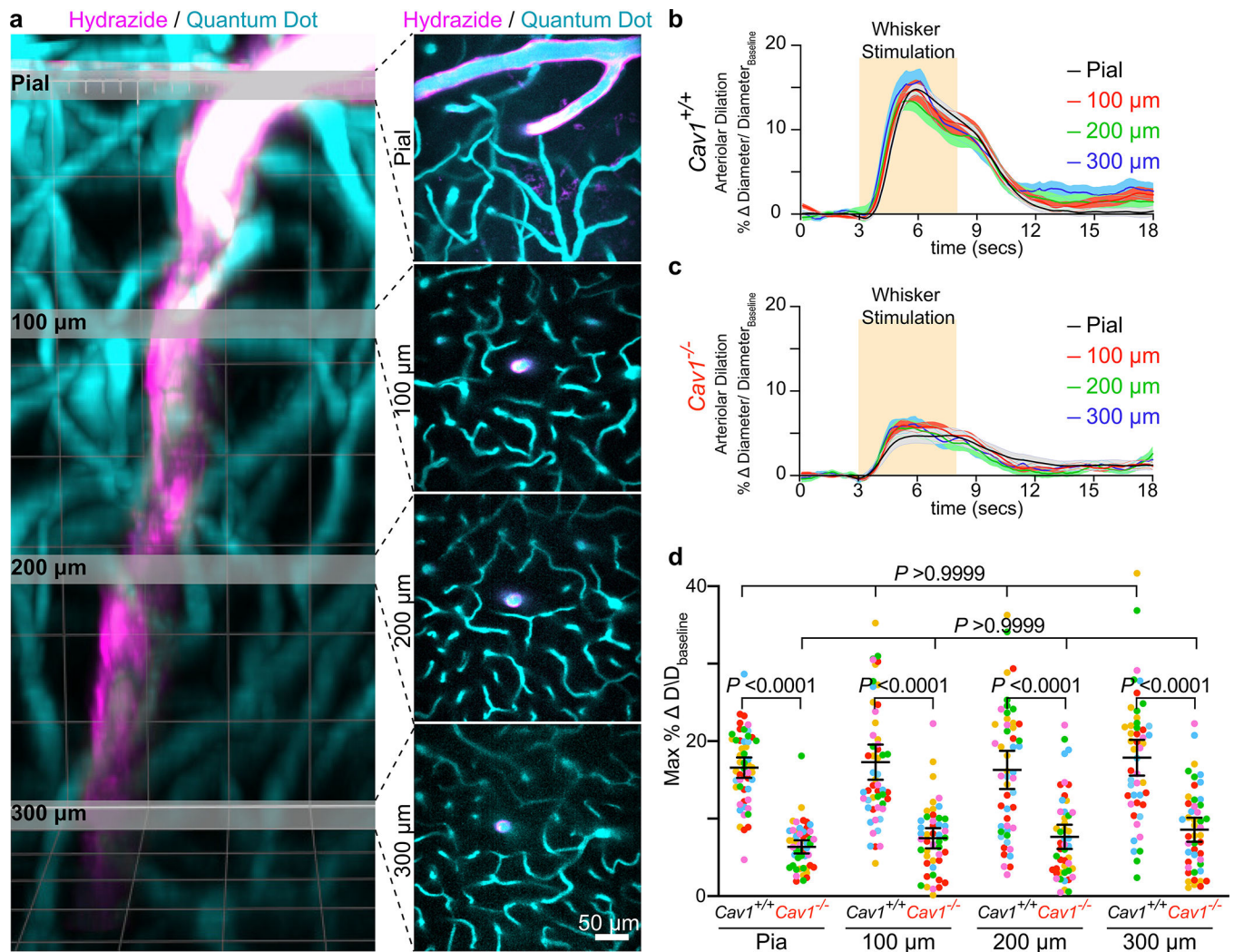
Extended Data Fig. 2. *Cav1* **knockout mice have impaired vasodilation in both pial arteries and penetrating arterioles diving deep into the parenchyma.**

a, 3D volume rendering of a two-photon imaged site in $Cav1^{+/+}$ mouse barrel cortex—from the pial surface to a depth of ~400 μm. The lumen of all vessels is filled with quantum dots (blue) and arterioles are labeled with Hydrazide (magenta). The reason the deepest imaged bin is at 300 μm because we see the appearance of the Hydrazide start at 300μm, indicating this is at the start of the arteriolar vessels. This observation is also consistent with a previous publication that characterized Hydrazide as an arteriolar vessel marker[5]. Gray slices correspond to z cross-sections shown per depth. Independent replications for (**a**) are performed in 5 wildtype mice. **b,c,** Time-course of change in arteriolar dilation in the barrel cortex from $Cav1^{+/+}$ (n= 5 mice, 10–15 arterioles per depth) (**b**) and $Cav1^{-/-}$ mice (n= 5 mice, 10–15 arterioles per depth) (**c**). **d,** Max % change in arteriolar dilation upon whisker stimulation between in $Cav1^{+/+}$ and $Cav1^{-/-}$ mice at the indicated depth. Statistical significance was determined by two-way ANOVA with a post hoc Bonferroni multiple comparison adjustment for (**d**). All data is mean ± s.e.m. We compared the max % change in arteriolar dilation upon whisker stimulation between $Cav1^{+/+}$ and $Cav1^{-/-}$ mice at each depth and also compared the responses across depth within the same genotype.
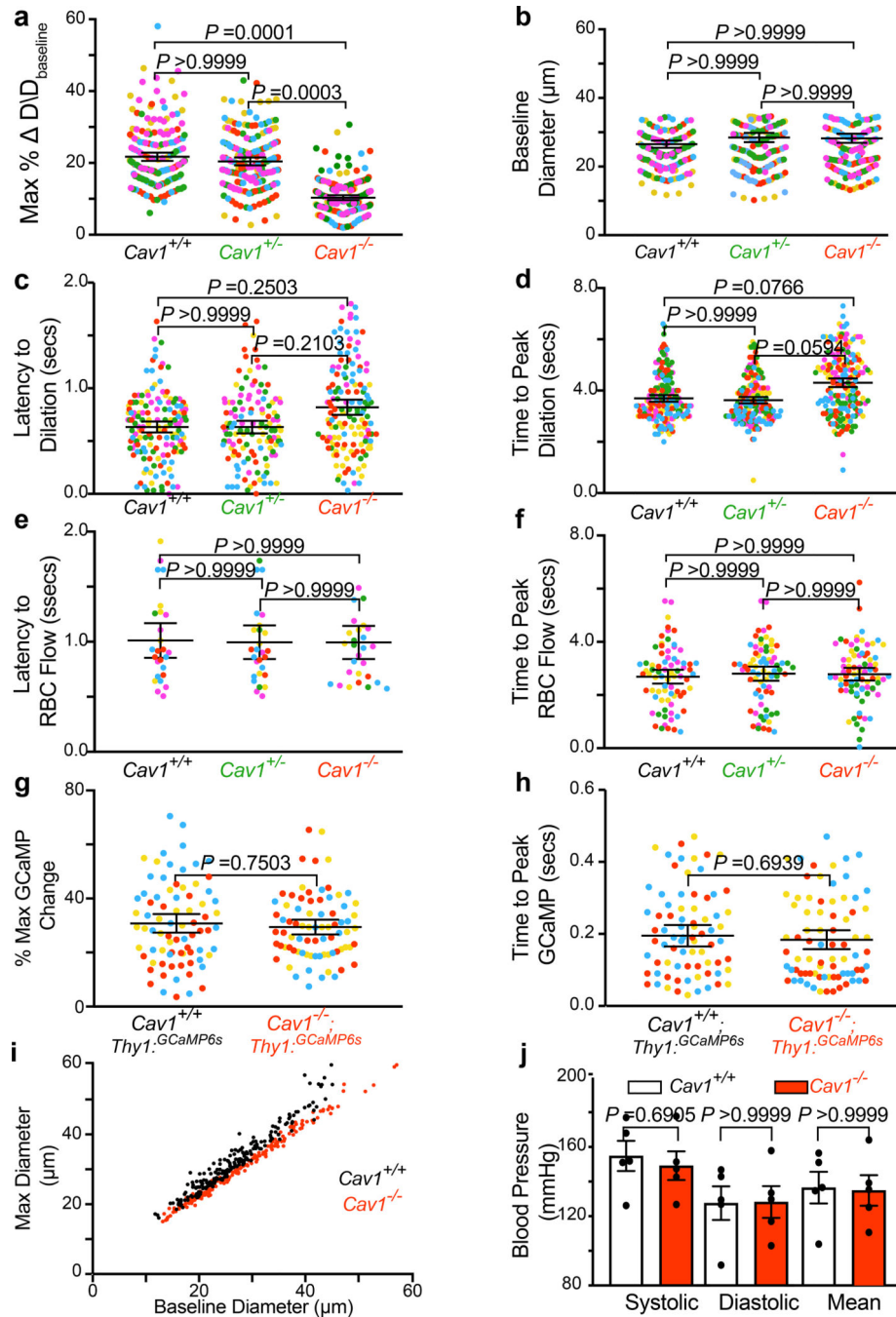
Extended Data Fig. 3. *Cav1* **knockout mice have attenuated vasodilation but normal neural activity and neurovascular coupling kinetics.**

a,b,c,d, max % change in dilation response (**a**), and baseline diameter (**b**) latency to max change in arteriolar dilation (**c**), time to peak dilation (**d**) in *Cav1*^{+/+} (n=193 arteries, 40 capillaries, 5 mice), *Cav1*^{+/−} (n= 123 arteries, 40 capillaries, 5 mice), *Cav1*^{−/−} mice (n=153 arteries, 31 capillaries, 5 mice). **e,f,** Latency to max RBC flow velocity (**e**) and time to peak RBC flow (**f**) in *Cav1*^{+/+} (n=193 arteries, 40 capillaries, 5 mice), *Cav1*^{+/−} (n= 123 arteries, 40 capillaries, 5 mice), *Cav1*^{−/−} mice (n=153 arteries, 31 capillaries, 5 mice). **g,h,** max %

change in GCaMP6s (**g**) and latency to peak change in GCaMPs (**h**) in $Cav1^{+/+}$; *Thy1:GCaMP6s* (n=78 field of views of the neuropils, 5 mice) and $Cav1^{-/-}$; *Thy1:GCaMP6s* (n=78 neuropils, 5 mice). Each circle represents an individual trial of GCaMP6s signal. **i,** Baseline diameter to absolute max diameter response during whisker stimulation in $Cav1^{+/+}$ and $Cav1^{-/-}$ mice. **j,** Tail-cuff blood pressure measurements between $Cav1^{+/+}$ (n= 5 mice) and $Cav1^{-/-}$ mice (n= 5 mice). Statistical significance was determined by a one-way nested ANOVA with a post hoc Bonferroni multiple comparison adjustment for (**a,b,c,d,e,f**), a nested unpaired, two-tailed t-test for (**g,h**), and two-tailed Mann–Whitney U test for (**j**). All data is mean ± s.e.m.
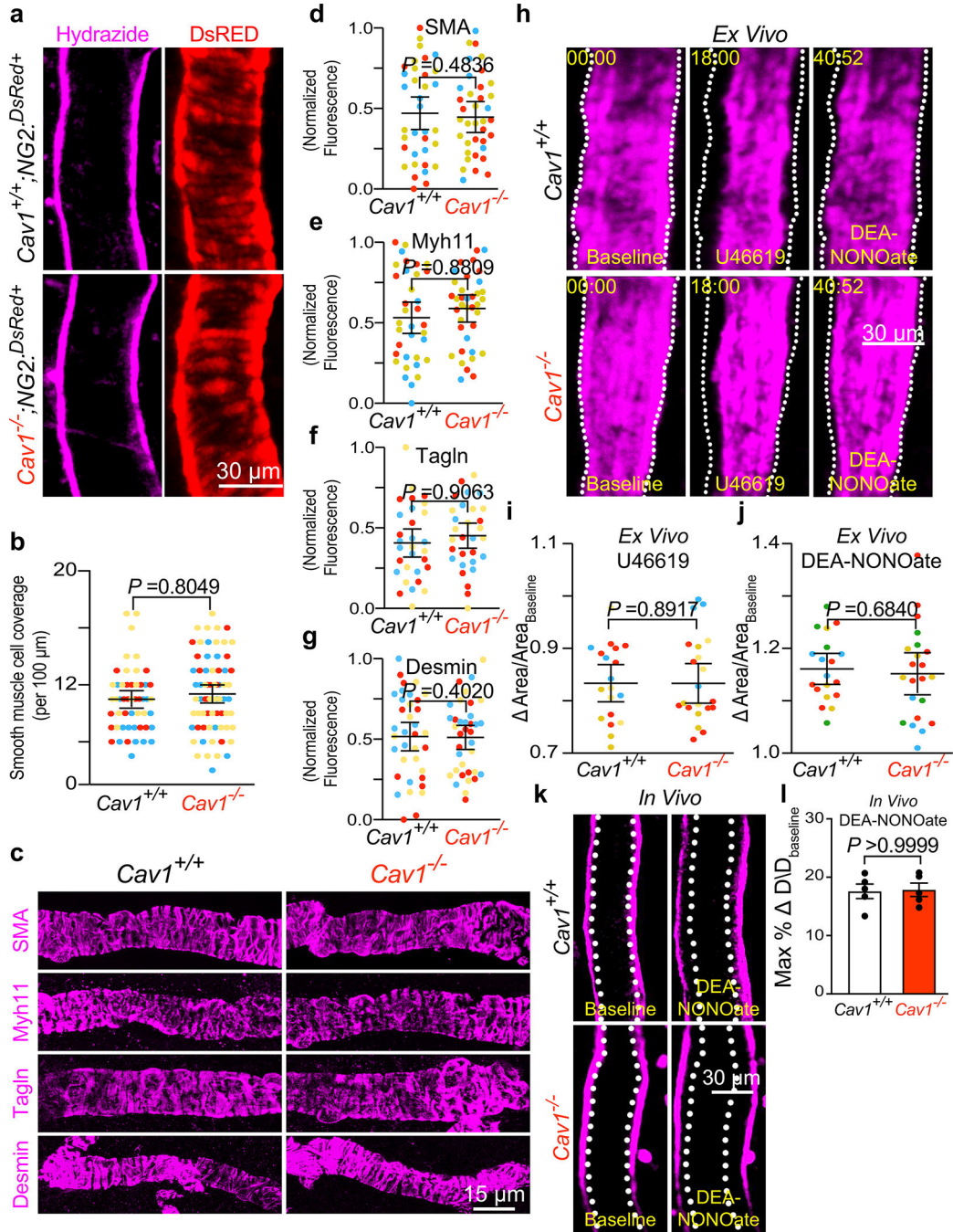
Extended Data Fig. 4. *Cav1* mutant mice exhibit normal smooth muscle cell integrity and function.
a, *In vivo* two-photon microscopy images of Hydrazide (magenta) and DsRed (red) from Cav1^{+/+}, NG2:[DsRED+] and Cav1^{−/−}, NG2:[DsRED+] mice. **b,** Quantification of DsRED+ smooth muscle cells per 100 μm as shown in (**a**) in *Cav1*^{+/+} (n= 3 mice, 27 arterioles) and *Cav1*^{−/−} (n= 3 mice, 28 arterioles). **c,** Immunostaining for SMC contractile proteins, including SMA, Myh11, Tagln and Desmin on brain arterioles from *Cav1*^{+/+} and *Cav1*^{−/−} mice. **d-g,** Normalized fluorescence quantification of the various contractile proteins from

$Cav1^{+/+}$ and $Cav1^{-/-}$ mice. **h,** Still frame images of arterioles labeled with Hydrazide (magenta) in *ex vivo* acute brain slices from $Cav1^{+/+}$ and $Cav1^{-/-}$ mice using two-photon microscopy. Left image shows arterioles during baseline, middle image shows during U46619 (thromboxane agonist) treatment and right image shows during DEA-NONOate (NO donor) treatment. White hashes outline the arterioles during baseline based on time = 0 min. **i,j,** Quantification of max arteriolar contraction by U46619 (**i**) and max arteriolar dilation by DEA-NONOate (**j**) on acute brain slices from $Cav1^{+/+}$ (n= 5 mice, 19 arterioles) and $Cav1^{-/-}$ (n= 5 mice, 22 arterioles). **k,** *in vivo* images of arterioles labeled with Hydrazide (magenta) from $Cav1^{+/+}$ and $Cav1^{-/-}$ mice using two-photon microscopy. Left image shows arterioles during baseline and right shows during DEA-NONOate superfusion. White hashes outline the arterioles during baseline based on time =0 sec. **l,** Quantification of max arteriolar dilation during DEA-NONOate superfusion *in vivo* (n= 5 mice for both genotypes). Statistical significance was determined by nested, unpaired, two-tailed t-test for (**b,d,e,f,g,i,j**) and by two-tailed Mann–Whitney U test for (**l**). Data shown as mean ± s.e.m.
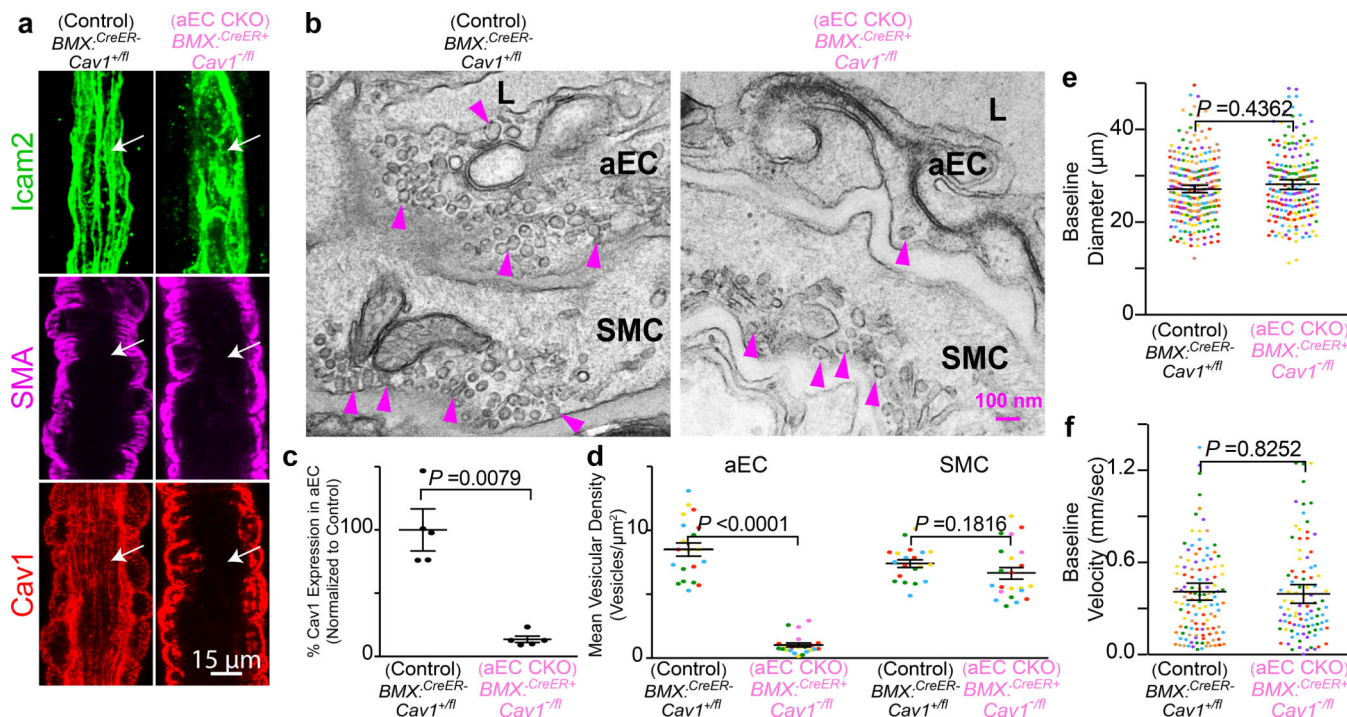
Extended Data Fig. 5. Caveolae in CNS aECs are abolished in aEC conditional *Cav1* knockout mice.

a, Immunostaining of adult brain sections for endothelial cells (Icam2, green), smooth muscle cells (SMA, magenta) and Cav1 (red) from control (*BMX:CreER−; Cav1+/fl*) and aEC-specific conditional Cav1 mutant (*BMX:CreER+; Cav1−/fl*) mice. Arrows point to aECs. **b,** EM images of CNS aECs and SMCs from control and aEC-specific conditional Cav1 mutant mice. Arrowheads point to caveolae. L, Lumen. aEC, arteriolar endothelial cells, SMC, smooth muscle cells. **c,** Quantification of mean normalized immunofluorescence of Cav1 in aECs from control (n= 5 mice) and aEC-specific conditional Cav1 mutant mice (n=5 mice). **d,** Quantification of the mean vesicular density in aECs and smooth muscle cells between control (n= 4 mice, 20 arterioles) and aEC-specific conditional Cav1 mutant mice (n=5 mice, 22 arterioles). Statistical significance was determined by Mann Whitney test for (**c**) and nested, unpaired, two-tailed t-test for (**d,e,f**). Data are shown as mean ± s.e.m.
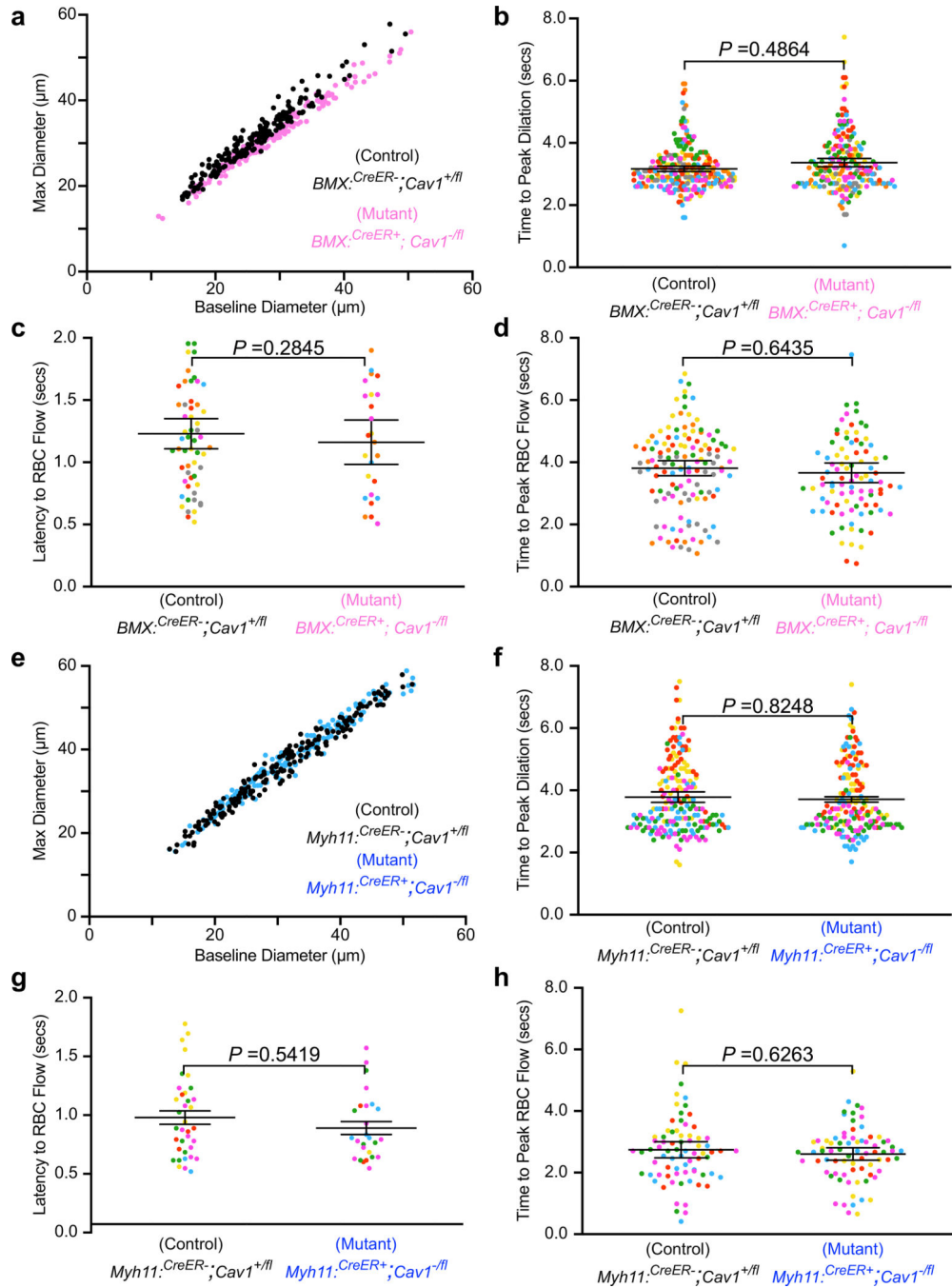
Extended Data Fig. 6. Conditional aEC-specific and SMC *Cav1* knockout mice have normal neurovascular coupling kinetics.

a, Baseline diameter to absolute max diameter response during whisker stimulation in control, *BMX:^{CreER-;} Cav1^{+/fl}*; and mutant, *BMX:^{CreER+;} Cav1^{−/fl}* mice. **b**, Quantification of time to peak arteriolar dilation in (*BMX:^{CreER-;} Cav1^{+/fl}*; n=7 mice, 234 arterioles) and aEC-specific conditional Cav1 mutant (*BMX:^{CreER+;} Cav1^{−/fl}*; n=5 mice; 202 arterioles) mice. **c,** Quantification of latency to peak RBC flow velocity in (*BMX:^{CreER−}; Cav1+/fl*; n n=7 mice; 58 capillaries) and aEC-specific conditional Cav1 mutant (*BMX:^{CreER+}; Cav1-/fl*; n=5 mice;

25 capillaries) mice. **d,** Quantification of time to peak RBC flow velocity in (BMX:$^{CreER-}$; $Cav1^{+/fl}$; n=7 mice, 127 capillaries) and aEC-specific conditional Cav1 mutant (BMX:$^{CreER+}$; $Cav1^{-/fl}$; n=5 mice; 94 capillaries) mice. **e,** Baseline diameter to absolute max diameter response during whisker stimulation in control, $Myh11$:$^{CreER-;}$ $Cav1^{+/fl}$; and mutant, $Myh11$:$^{CreER+;}$ $Cav1^{-/fl}$ mice. **f,** Quantification of time to peak arteriolar dilation in ($Myh11$:$^{CreER-}$; $Cav1^{+/fl}$; n=5 mice, 193 arterioles) and SMC conditional Cav1 mutant ($Myh11$:$^{CreER+}$; $Cav1^{-/fl}$; n=5 mice; 180 arterioles) mice. **g,** Quantification of latency to RBC flow in ($Myh11$:$^{CreER-}$; $Cav1^{+/fl}$; n=5 mice; 36 capillaries) and SMC conditional Cav1 mutant ($Myh11$:$^{CreER+}$; $Cav1^{-/fl}$; n=5 mice; 26 capillaries) mice. **h,** Quantification time to peak RBC flow velocity in ($Myh11$:$^{CreER-}$; $Cav1^{+/fl}$; n=5 mice; 75 capillaries) and SMC conditional Cav1 mutant ($Myh11$:$^{CreER+}$; $Cav1^{-/fl}$; n=5 mice; 75 capillaries) mice. Statistical significance was determined by a nested unpaired, two-tailed t-test for (**b-d** and **f-h**).
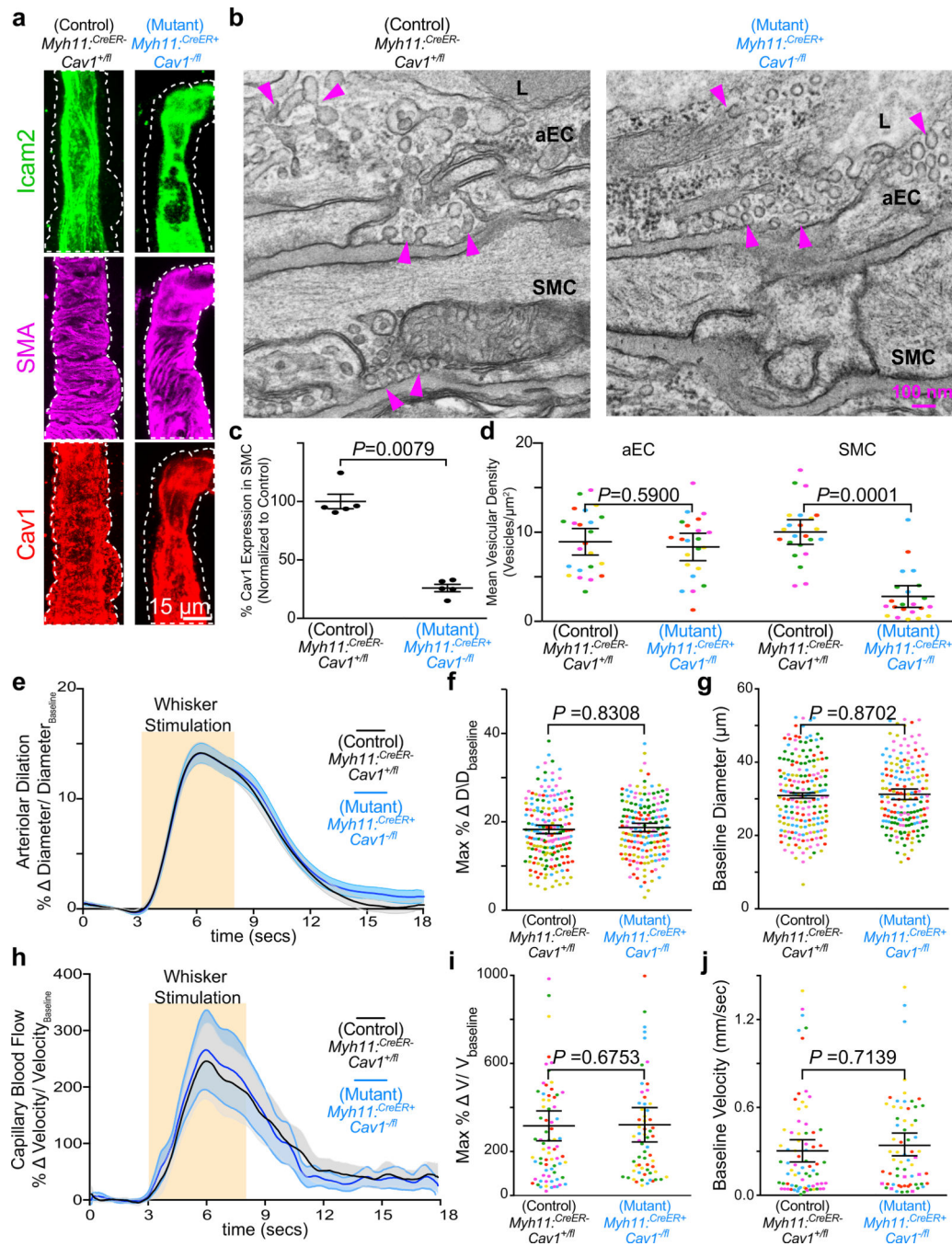
Extended Data Fig. 7. Conditional SMC-specific *Cav1* knockout mice have normal neurovascular coupling.

a, Immunostaining on brain sections for endothelial cells (Icam2, green), smooth muscle cells (SMA, magenta) and Cav1 (red) from control and SMC conditional Cav1 mutant mice. **b,** EM images of CNS aECs and SMCs from control and SMC conditional *Cav1* mutant mice. Arrowheads point to caveolae. L, Lumen. aEC, arteriolar endothelial cells. SMC, smooth muscle cells. **c,** Quantification of mean normalized immunofluorescence of Cav1 in SMCs from control (n= 5 mice) and SMC-specific conditional *Cav1* mutant mice (n=5

mice). **d**, Quantification of the mean vesicular density in aECs and smooth muscle cells between control (n= 5 mice, 23 arterioles) and SMC conditional $Cav1^{-/-}$ mutant mice (n=5 mice, 22 arterioles). **e,f,g,** Time-course of change in arteriolar dilation (**e**), max % change in arteriolar dilation (**f**) and baseline diameter (**g**) in control (n= 7 mice, 193 arterioles) and SMC conditional $Cav1$ mutant mice (n= 5 mice, 176 arterioles). **h,i,j,** Time-course of change in red blood cell velocity (**h**), max % change in red blood cell velocity (**i**) and baseline velocity (**j**) in control (n= 7 mice, 75 capillaries) and SMC conditional $Cav1$ mutant mice (n=5 mice, 64 capillaries). Statistical significance was determined by unpaired, two-tailed Mann–Whitney U test for (**c**) and a nested, unpaired, two-tailed t-test for (**d,f,g,i,j**). Data shown as mean ± s.e.m.
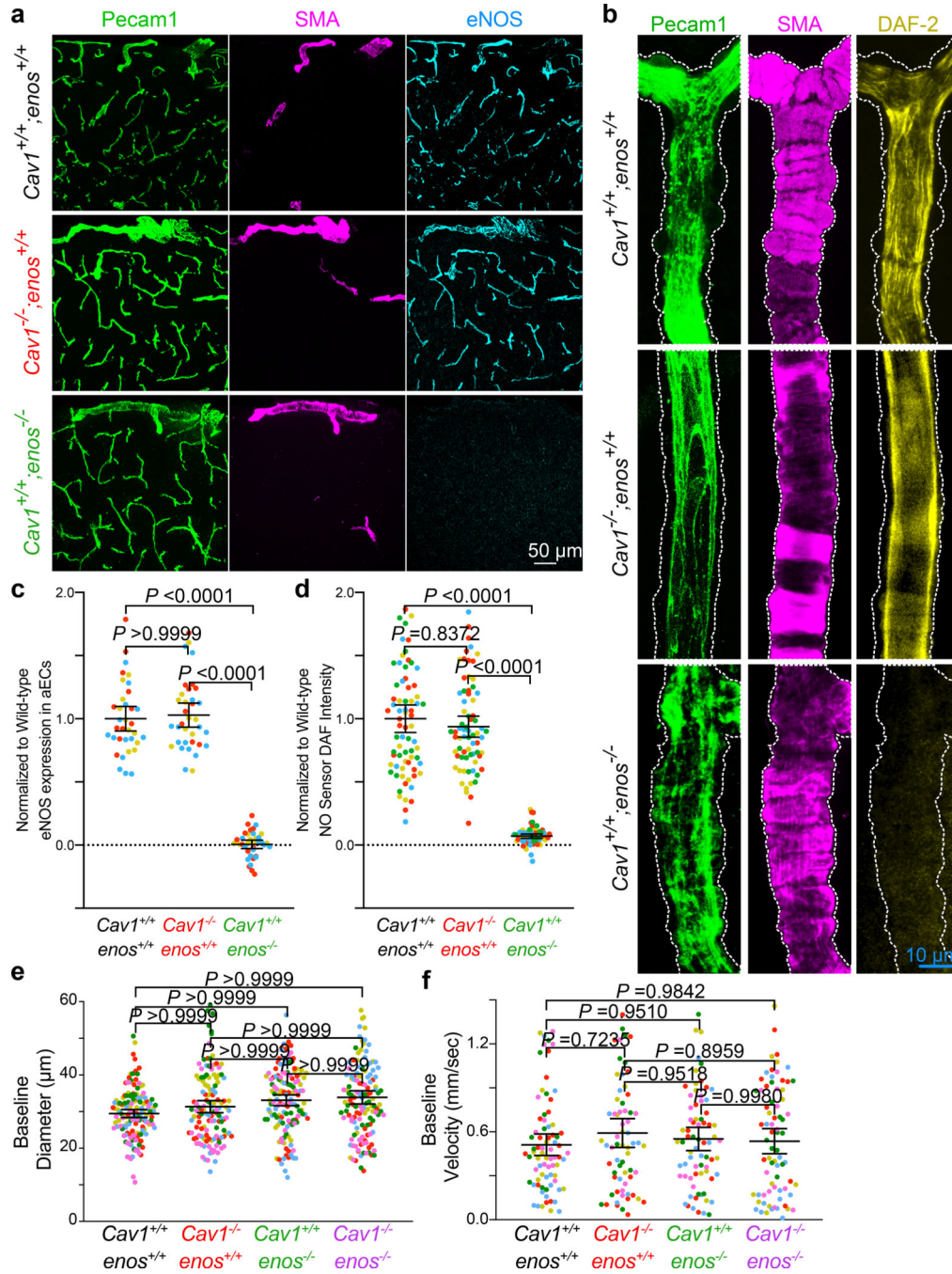
Extended Data Fig. 8. *Cav1* **mutant mice have normal levels of eNOS protein and NO in CNS aECs and** *Cav1, eNOS* **double knockout have normal baseline diameter and red blood cell flow.**
a, Immunostaining on adult brain sections for endothelial cells (Pecam1, green), arterioles (SMA, magenta) and eNOS (cyan) from $Cav1^{+/+}$, $enos^{+/+}$, $Cav1^{-/-}$, $enos^{+/+}$ and $Cav1^{+/+}$, $enos^{-/-}$ mice. Independent replications were performed on 3 mice per genotype. **b,** Immunostaining for (Pecam1, green) and arterioles (SMA, magenta) on brain sections from $Cav1^{+/+}$, $enos^{+/+}$, $Cav1^{-/-}$, $enos^{+/+}$ and $Cav1^{+/+}$, $enos^{-/-}$ mice after *in vivo* perfusion of NO sensitive dye- DAF-2, yellow. Independent replications were performed on 4 mice per

genotype. **c,** Quantification of eNOS immunofluorescence intensity as shown in (**a**) in aECs from $Cav1^{+/+}$, $enos^{+/+}$ (n= 3 mice, 35 images), $Cav1^{-/-}$, $enos^{+/+}$ (n= 3 mice, 35 images), and $Cav1^{+/+}$, $enos^{-/-}$ (n= 3 mice, 37 images). **d,** Quantification of DAF-2 intensity in aECs as shown in (**b**) from $Cav1^{+/+}$, $enos^{+/+}$ (n= 4 mice, 73 images), $Cav1^{-/-}$, $enos^{+/+}$ (n= 4 mice, 71 images), and $Cav1^{+/+}$, $enos^{-/-}$ (n= 4 mice, 64 images). **e,f,** Quantification of baseline diameter (**e**) and baseline velocity (**f**) in $Cav1^{+/+}$, $enos^{+/+}$ (n= 5 mice, 148 arterioles, 76 capillaries), $Cav1^{-/-}$, $enos^{+/+}$ (n= 5 mice, 128 arterioles, 68 capillaries), $Cav1^{+/+}$, $enos^{-/-}$ (n= 5 mice, 137 arterioles, 73 capillaries) and $Cav1^{-/-}$, $enos^{-/-}$ mice (n=5 mice, 139 arterioles, 74 capillaries). Statistical significance was determined by nested, unpaired, two-tailed t-test for (**c,d**) and nested, one-way ANOVA with a post hoc Bonferroni multiple comparison adjustment for (**e,f**). Data shown as mean ± s.e.m.
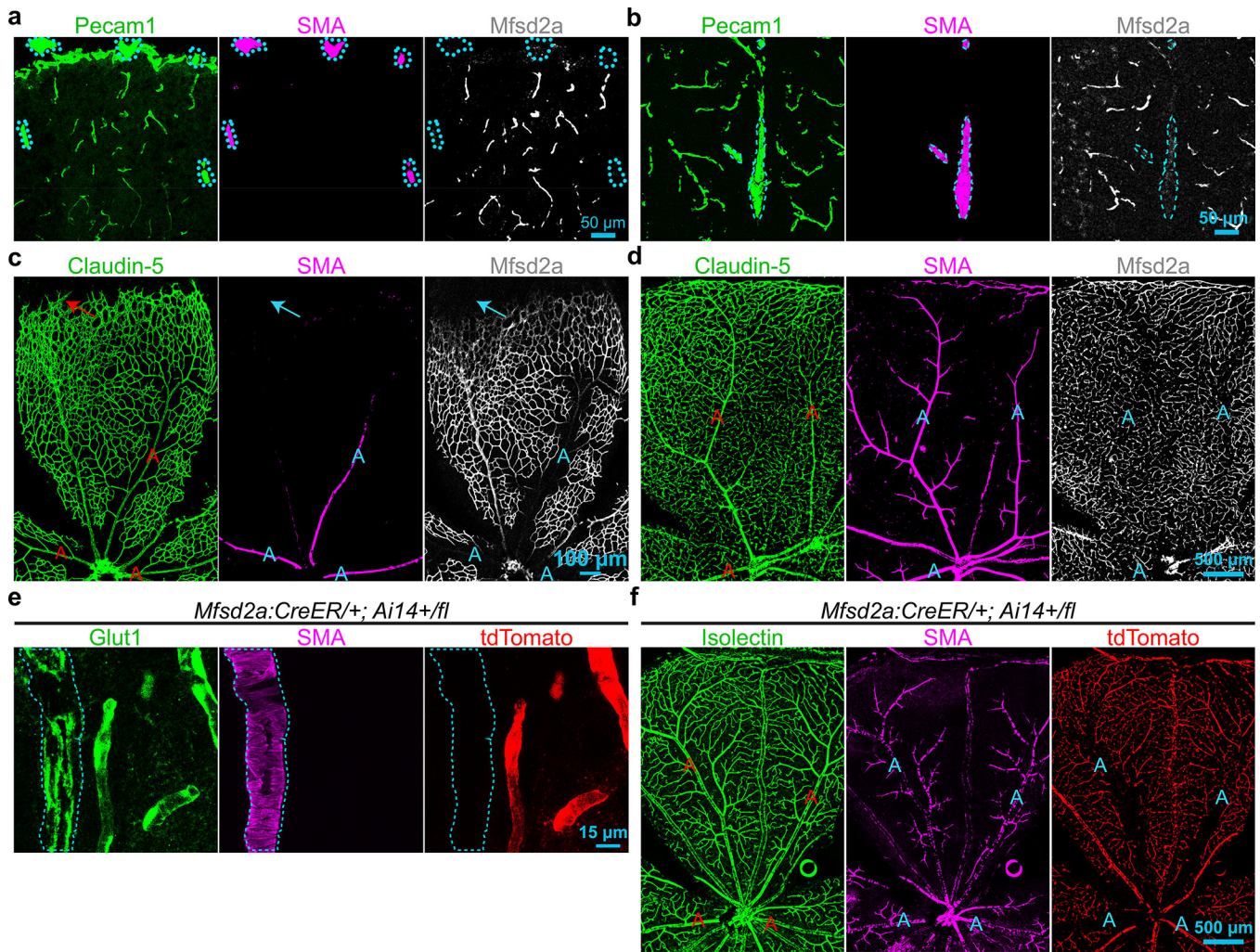
Extended Data Fig. 9. Mfsd2a is undetected in CNS arterioles in brain and retina.
a,b, Immunostaining on P5 (**a**) and adult (**b**) brain sections for endothelial cells (Pecam1, green), smooth muscle cells (SMA, magenta) and Mfsd2a (white) from wildtype mice. Blue hashes outline SMA+ arterioles. **c,d,** Immunostaining on P5 (**c**) and adult (**d**) retina for endothelial cells (Claudin-5, green), smooth muscle cells (SMA, magenta) and Mfsd2a (white) from wildtype mice. A- arterioles. Note that Mfsd2a is absent in nascent, distal vessel (arrows) in P5 retina in (**c**). **e,f,** Tamoxifen-treated, adult knock-in Mfsd2a:$^{CreER+}$; Ai14$^{+/fl}$ reporter mice demonstrates that tdTomato is absent in SMA+ arterioles but present in SMA- capillaries in brain (**e**) and retina (**f**). Blue hashes and "A" indicate SMA+ arterioles. Independent replications for (**a-f**) were done on 5 wildtype mice.
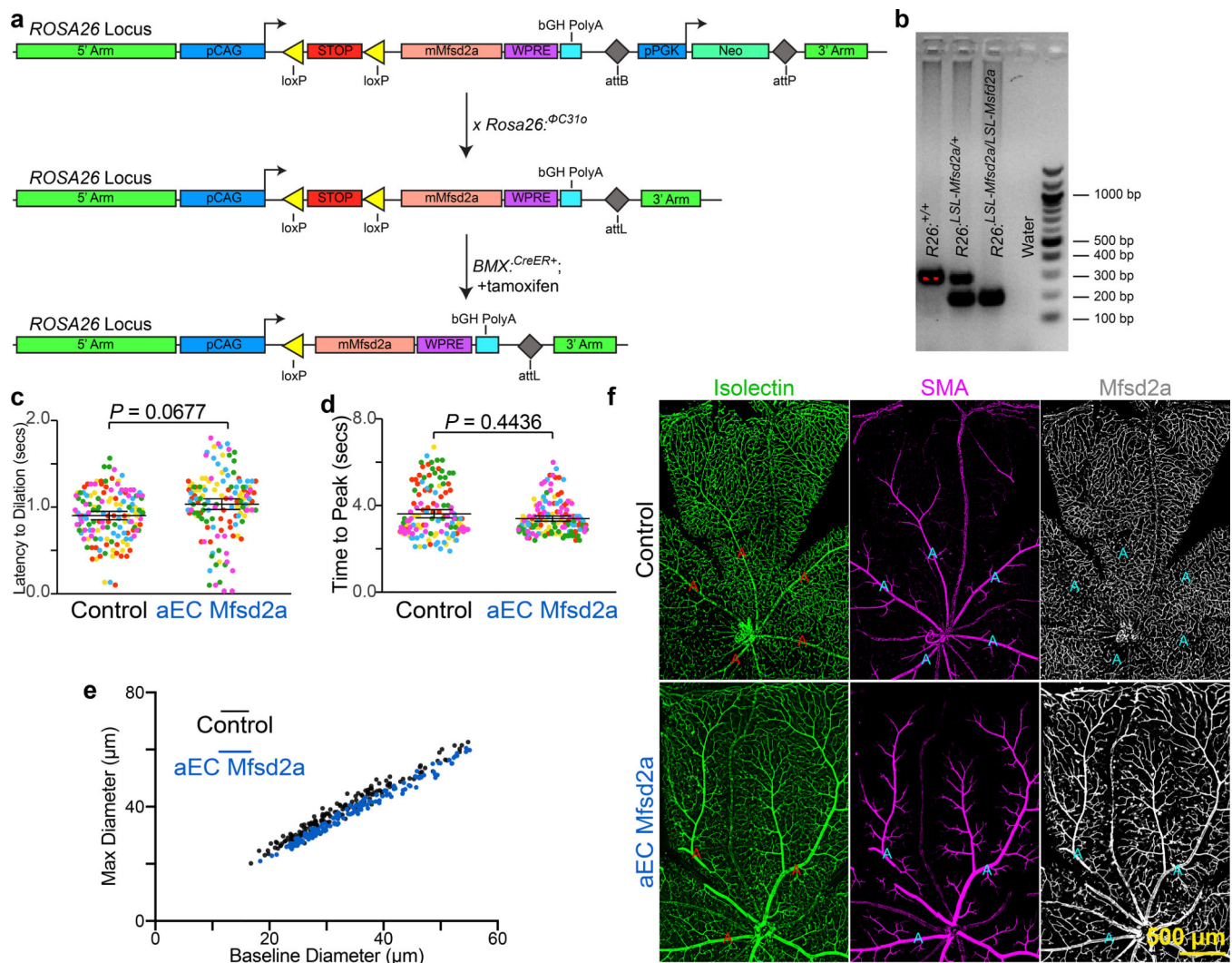
Extended Data Fig. 10. Generation of a Cre-dependent Mfsd2a overexpression transgenic mouse ($R26$:$^{LSL-Mfsd2a}$).

a, Construct of the Cre-dependent Mfsd2a overexpression knocked-in to the ROSA26 locus. Mating with *ROSA26: ΦC31* recombinase mice removes the neomycin selection cassette. Subsequent mating with *BMX:CreER* and tamoxifen injection allows ectopic overexpression of Mfsd2a in aECs. **b,** PCR genotyping of Cre-dependent Mfsd2a overexpression mice. **c,** Quantification of latency to changes in arteriolar dilation in control (*BMX:*$^{CreER-}$; *R26:*$^{LSL-Mfsd2a/+}$; n=5 mice, 149 arterioles) and aEC-specific Mfsd2a overexpression (*BMX:*$^{CreER+}$; *R26:*$^{LSL-Mfsd2a/+}$; n=5 mice; 138 arterioles) mice. **d,** Quantification of time to peak arteriolar dilation in (*BMX:*$^{CreER-}$; *R26:*$^{LSL-Mfsd2a/+}$; n=5 mice, 149 arterioles) and aEC-specific conditional Cav1 mutant (*BMX:*$^{CreER+}$; *R26:*$^{LSL-Mfsd2a/+}$; n=5 mice; 138 arterioles) mice. **e,** Baseline diameter to absolute max diameter response during whisker stimulation in control, (*BMX:*$^{CreER-}$; *R26:*$^{LSL-Mfsd2a/+}$; n=5 mice, 149 arterioles); and (*BMX:*$^{CreER+}$; *R26:*$^{LSL-Mfsd2a/+}$; n=5 mice; 138 arterioles) mice. **f,** Immunostaining on adult retinas for endothelial cells (isolectin, green), smooth muscle cells (SMA, magenta) and Mfsd2a (white) from control and aEC-specific Mfsd2a overexpression mice. Independent

replications for (**f**) were done on 3 mice per genotype. Statistical significance was determined by a nested unpaired, two-tailed t-test for (**c** and **d**).

Supplementary Material

Refer to Web version on PubMed Central for supplementary material.

Acknowledgments

References

1. Iadecola C The Neurovascular Unit Coming of Age: A Journey through Neurovascular Coupling in Health and Disease. Neuron 96, 17–42 (2017). [PubMed: 28957666]

2. Hillman EMC Coupling mechanism and significance of the BOLD signal: a status report. Annu. Rev. Neurosci. 37, 161–181 (2014). [PubMed: 25032494]

3. Sweeney MD, Sagare AP & Zlokovic BV Blood-brain barrier breakdown in Alzheimer disease and other neurodegenerative disorders. Nat Rev Neurol 14, 133–150 (2018). [PubMed: 29377008]

4. Kleinfeld D et al. A guide to delineate the logic of neurovascular signaling in the brain. Frontiers in neuroenergetics 3, 1 (2011). [PubMed: 21559095]

5. Shen Z, Lu Z, Chhatbar PY, O'Herron P & Kara P An artery-specific fluorescent dye for studying neurovascular coupling. Nat. Methods 9, 273–276 (2012). [PubMed: 22266543]

6. Chen BR, Kozberg MG, Bouchard MB, Shaik MA & Hillman EMC A critical role for the vascular endothelium in functional neurovascular coupling in the brain. J Am Heart Assoc 3, e000787 (2014). [PubMed: 24926076]

7. O'Herron P et al. Neural correlates of single-vessel haemodynamic responses in vivo. Nature 534, 378–382 (2016). [PubMed: 27281215]

8. Longden TA et al. Capillary K(+)-sensing initiates retrograde hyperpolarization to increase local cerebral blood flow. Nat. Neurosci 20, 717–726 (2017). [PubMed: 28319610]

9. Hogan-Cann AD, Lu P & Anderson CM Endothelial NMDA receptors mediate activity-dependent brain hemodynamic responses in mice. Proc. Natl. Acad. Sci. U.S.A 116, 10229–10231 (2019). [PubMed: 31061120]

10. Ben-Zvi A et al. Mfsd2a is critical for the formation and function of the blood-brain barrier. Nature 509, 507–511 (2014). [PubMed: 24828040]

11. Chow BW & Gu C Gradual Suppression of Transcytosis Governs Functional Blood-Retinal Barrier Formation. Neuron 93, 1325–1333.e3 (2017). [PubMed: 28334606]

12. Andreone BJ et al. Blood-Brain Barrier Permeability Is Regulated by Lipid Transport-Dependent Suppression of Caveolae-Mediated Transcytosis. Neuron 94, 581–594.e5 (2017). [PubMed: 28416077]

13. Razani B et al. Caveolin-1 null mice are viable but show evidence of hyperproliferative and vascular abnormalities. J. Biol. Chem 276, 38121–38138 (2001). [PubMed: 11457855]

14. Drab M et al. Loss of caveolae, vascular dysfunction, and pulmonary defects in caveolin-1 gene-disrupted mice. Science 293, 2449–2452 (2001). [PubMed: 11498544]

15. Simionescu M et al. The cerebral microvasculature of the rat: structure and luminal surface properties during early development. Journal of submicroscopic cytology and pathology 20, 243–261 (1988). [PubMed: 3395964]

16. Hill RA et al. Regional Blood Flow in the Normal and Ischemic Brain Is Controlled by Arteriolar Smooth Muscle Cell Contractility and Not by Capillary Pericytes. Neuron 87, 95–110 (2015). [PubMed: 26119027]

17. Lim DH et al. In vivo Large-Scale Cortical Mapping Using Channelrhodopsin-2 Stimulation in Transgenic Mice Reveals Asymmetric and Reciprocal Relationships between Cortical Areas. Front Neural Circuits 6, 11 (2012). [PubMed: 22435052]

18. Rosengren B-I et al. Transvascular protein transport in mice lacking endothelial caveolae. American Journal of Physiology - Heart and Circulatory Physiology 291, H1371–7 (2006). [PubMed: 16501011]

19. Zhu X, Bergles DE & Nishiyama A NG2 cells generate both oligodendrocytes and gray matter astrocytes. Development (Cambridge, England) 135, 145–157 (2008).

20. Ehling M, Adams S, Benedito R & Adams RH Notch controls retinal blood vessel maturation and quiescence. Development (Cambridge, England) 140, 3051–3061 (2013).

21. Asterholm IW, Mundy DI, Weng J, Anderson RGW & Scherer PE Altered mitochondrial function and metabolic inflexibility associated with loss of caveolin-1. Cell Metab. 15, 171–185 (2012). [PubMed: 22326219]

22. Wirth A et al. G12-G13-LARG-mediated signaling in vascular smooth muscle is required for salt-induced hypertension. Nat. Med 14, 64–68 (2008). [PubMed: 18084302]

23. Parton RG Caveolae: Structure, Function, and Relationship to Disease. Annu. Rev. Cell Dev. Biol 34, 111–136 (2018). [PubMed: 30296391]

24. Sinha B et al. Cells respond to mechanical stress by rapid disassembly of caveolae. Cell 144, 402–413 (2011). [PubMed: 21295700]

25. Balijepalli RC & Kamp TJ Caveolae, ion channels and cardiac arrhythmias. Progress in Biophysics and Molecular Biology 98, 149–160 (2008). [PubMed: 19351512]

26. Sowa G, Pypaert M & Sessa WC Distinction between signaling mechanisms in lipid rafts vs. caveolae. PNAS 98, 14072–14077 (2001). [PubMed: 11707586]

27. Toth P et al. Purinergic glio-endothelial coupling during neuronal activity: role of P2Y1 receptors and eNOS in functional hyperemia in the mouse somatosensory cortex. American Journal of Physiology - Heart and Circulatory Physiology 309, H1837–H1845 (2015). [PubMed: 26453330]

28. García-Cardeña G et al. Dissecting the interaction between nitric oxide synthase (NOS) and caveolin. Functional significance of the nos caveolin binding domain in vivo. J. Biol. Chem 272, 25437–25440 (1997). [PubMed: 9325253]

29. Vanlandewijck M et al. A molecular atlas of cell types and zonation in the brain vasculature. Nature 554, 475–480 (2018). [PubMed: 29443965]

30. Goedicke-Fritz S et al. Evidence for functional and dynamic microcompartmentation of Cav-1/TRPV4/KCa in caveolae of endothelial cells. European Journal of Cell Biology 94, 391–400 (2015). [PubMed: 26116074]

Method References

31. Pu W et al. Mfsd2a+ hepatocytes repopulate the liver during injury and regeneration. Nat Commun 7, 13369 (2016). [PubMed: 27857132]

32. Madisen L et al. A robust and high-throughput Cre reporting and characterization system for the whole mouse brain. Nat. Neurosci 13, 133–140 (2010). [PubMed: 20023653]

33. Madisen L et al. A toolbox of Cre-dependent optogenetic transgenic mice for light-induced activation and silencing. Nat. Neurosci 15, 793–802 (2012). [PubMed: 22446880]

34. Quina LA, Harris J, Zeng H & Turner EE Specific connections of the interpeduncular subnuclei reveal distinct components of the habenulopeduncular pathway. Journal of Comparative Neurology 525, 2632–2656 (2017). [PubMed: 28387937]

35. Chen T-W et al. Ultrasensitive fluorescent proteins for imaging neuronal activity. Nature 499, 295–300 (2013). [PubMed: 23868258]

36. Shesely EG et al. Elevated blood pressures in mice lacking endothelial nitric oxide synthase. PNAS 93, 13176–13181 (1996). [PubMed: 8917564]

37. Raymond CS & Soriano P High-efficiency FLP and PhiC31 site-specific recombination in mammalian cells. PLoS ONE 2, e162 (2007). [PubMed: 17225864]

38. Steger C An Unbiased Detector of Curvilinear Structures. Ieee Transactions On Pattern Analysis And Machine Intelligence 20, 1–13 (1998).

39. Chhatbar PY & Kara P Improved blood velocity measurements with a hybrid image filtering and iterative Radon transform algorithm. Front Neurosci 7, 106 (2013). [PubMed: 23807877]

40. Nguyen LN et al. Mfsd2a is a transporter for the essential omega-3 fatty acid docosahexaenoic acid. Nature 509, 503–506 (2014). [PubMed: 24828044]

41. Kanetsuna Y et al. Deficiency of Endothelial Nitric-Oxide Synthase Confers Susceptibility to Diabetic Nephropathy in Nephropathy-Resistant Inbred Mice. Am. J. Pathol 170, 1473–1484 (2007). [PubMed: 17456755]

42. Jiang R et al. Generation of a conditional allele for the mouse endothelial nitric oxide synthase gene. Genesis 50, 685–692 (2012). [PubMed: 22467476]
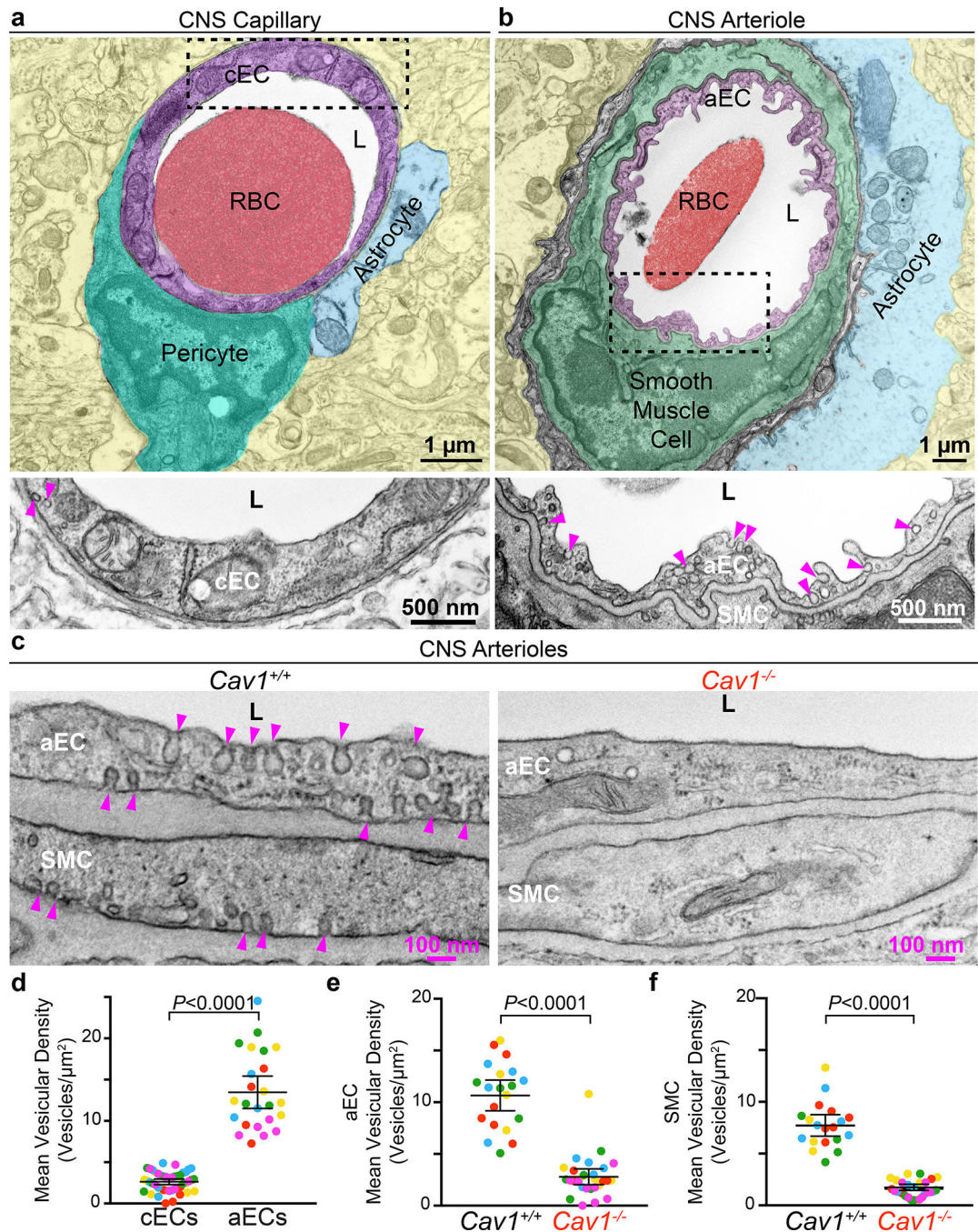
Fig 1. CNS arterioles have abundant caveolae.

a, EM image of a CNS capillary. Pseudocolors highlight different cells: capillary endothelial cell (cEC) (purple), pericyte (teal), astrocyte end-foot (blue), red blood cell (RBC, red), lumen (L, white) and neuropil (yellow). Bottom shows an inverted, zoomed image of the boxed area in cEC. **b,** EM image of a CNS arteriole. Pseudocolors highlight different cells: aEC (purple), smooth muscle cell (SMC, green), astrocyte end-foot (blue) and neuropil (yellow). Bottom shows a zoomed image of boxed area in aEC. Arrowheads point to vesicles in (**a,b**). **c,** EM images of aECs and SMCs from *Cav1*^{+/+} and *Cav1*^{−/−} mice. Arrowheads

point to caveolae. **d,** Quantification of the mean vesicular density between cECs and aECs from wildtype mice (n = 5 mice, 46 capillaries and 24 arterioles). **e,f,** Quantification of the mean vesicular density in aECs (**e**) and SMCs (**f**) between $CavI^{+/+}$ (n=5 mice, 20 arterioles) and $CavI^{-/-}$ mice (n=5 mice, 28 arterioles). Statistical significance was determined by nested, unpaired, two-tailed t-test for (**d,e,f**). Data are shown as mean ± s.e.m.
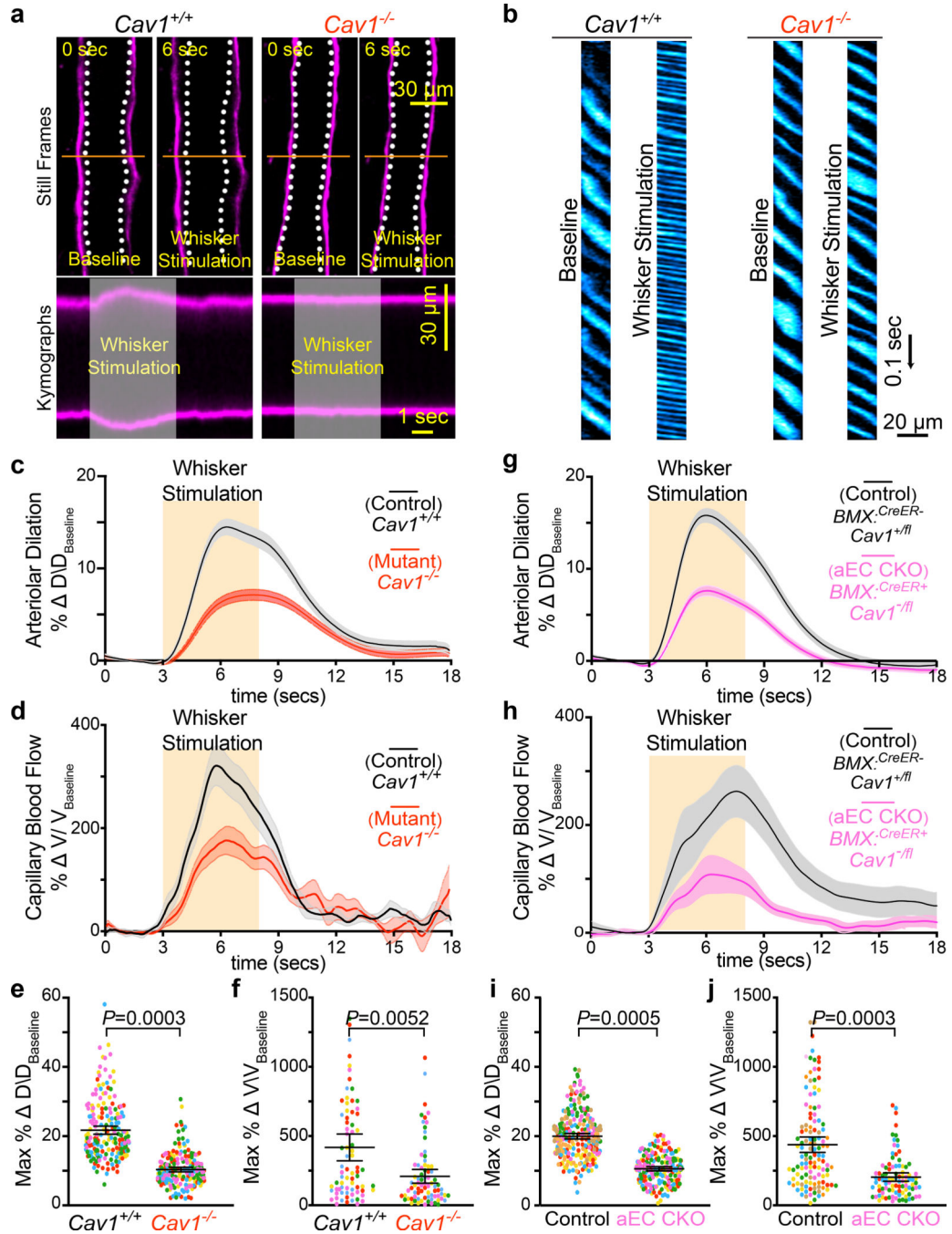
Fig 2. Caveolae in CNS aECs specifically are required for neurovascular coupling.
a, Still frame images of pial arteries during neurovascular coupling in $Cav1^{+/+}$ and $Cav^{-/-}$ mice using *in vivo* two-photon microscopy. Top images show Hydrazide-stained arterioles during baseline and whisker stimulation. White hashes outline the arterioles during baseline period. Bottom images show the kymographs of the arteriolar dilation, which were generated by transverse line scans (orange lines in top images). The gray rectangle in the kymograph represents the whisker stimulation period. **b,** Kymographs of RBC flow in capillaries for $Cav1^{+/+}$ and $Cav1^{-/-}$ mice. Dark streaks represent red blood cells, blue streaks represent the

fluorescent tracer-filled capillary lumen. Left and right kymographs show RBC flow during baseline and whisker stimulation, respectively. Independent replications for (**a**) and (**b**) are listed in (**c**) and (**d**) respectively. **c,d,e,f,** Time-course of change in arteriolar dilation (**c**), change in red blood cell velocity (**d**), max % change in arteriolar dilation (**e**) and red blood cell velocity (**f**) in in $Cav1^{+/+}$ (n= 5 mice, 196 arterioles, 77 capillaries) and $Cav1^{-/-}$ mice (n=5 mice, 194 arterioles, 79 capillaries). **g,h,i,j,** Time-course of change in arteriolar dilation (**g**), change in red blood cell velocity (**h**), max % change in arteriolar dilation (**i**) and red blood cell velocity (**j**) in control ($BMX^{:CreER-};Cav1^{+/fl}$; n= 7 mice, 260 arterioles, 122 capillaries) and aEC conditional $Cav1$ knockout mice ($BMX^{:CreER+};Cav1^{-/fl}$; n= 5 mice, 193 arterioles, 94 capillaries). Statistical significance was determined by nested, unpaired, two-tailed t-test for for (**e,f,i,j**). Data are shown as mean ± s.e.m.
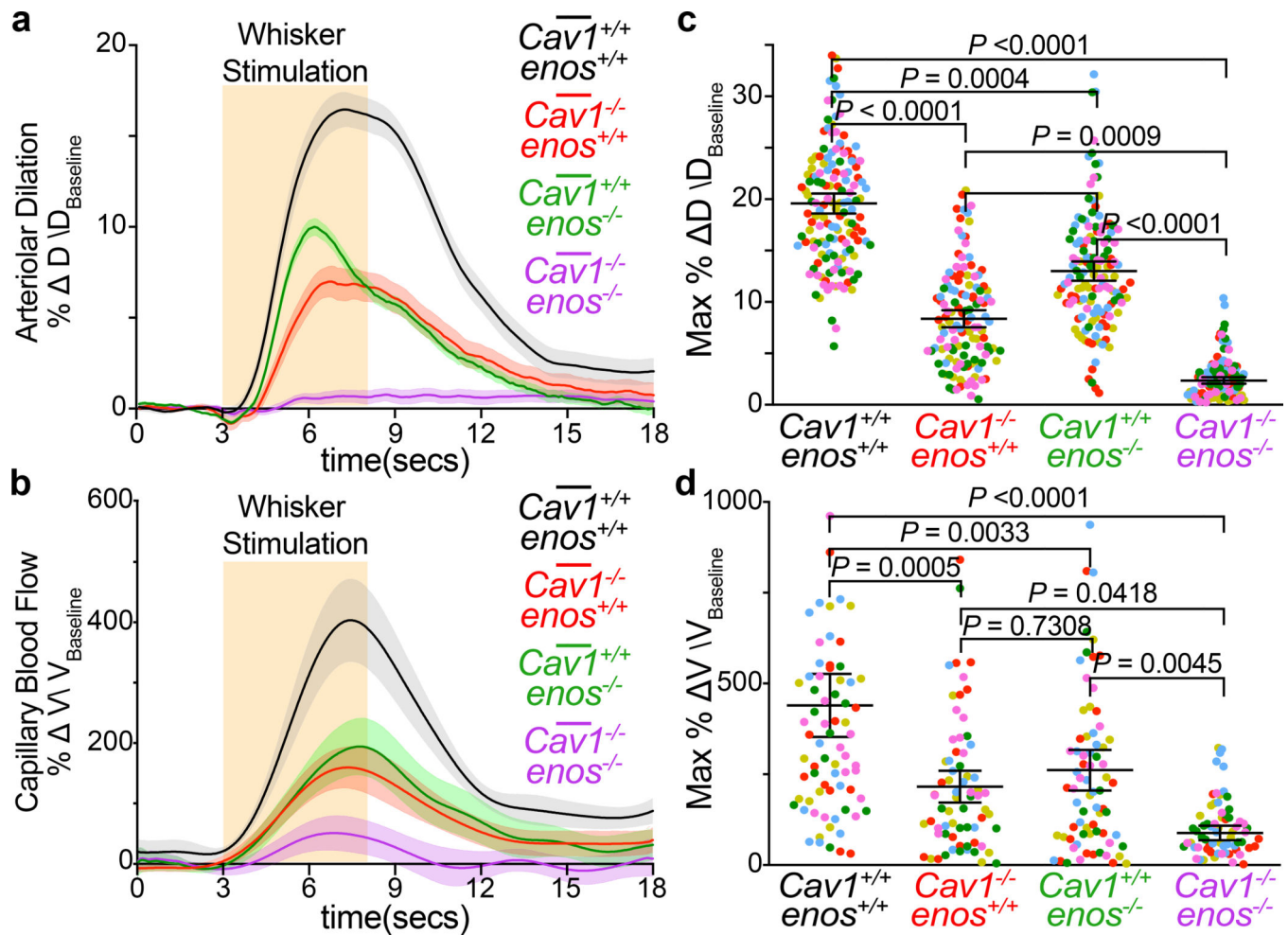
Figure 3. Caveolae in aECs mediate neurovascular coupling independently of eNOS.
Time-course of change in arteriolar dilation (**a**), change in red blood cell velocity (**b**), max %
change in arteriolar dilation (**c**) and red blood cell velocity (**d**) in $Cav1^{+/+}$, $enos^{+/+}$ (n= 5
mice, 148 arterioles, 76 capillaries), $Cav1^{-/-}$, $enos^{+/+}$ (n= 5 mice, 128 arterioles, 68
capillaries), $Cav1^{+/+}$, $enos^{-/-}$ (n= 5 mice, 137 arterioles, 73 capillaries) and $Cav1^{-/-}$, $enos^{-/-}$
mice (n=5 mice, 139 arterioles, 74 capillaries). Statistical significance was determined by
nested, one-way ANOVA with a post hoc Bonferroni multiple comparison adjustment for
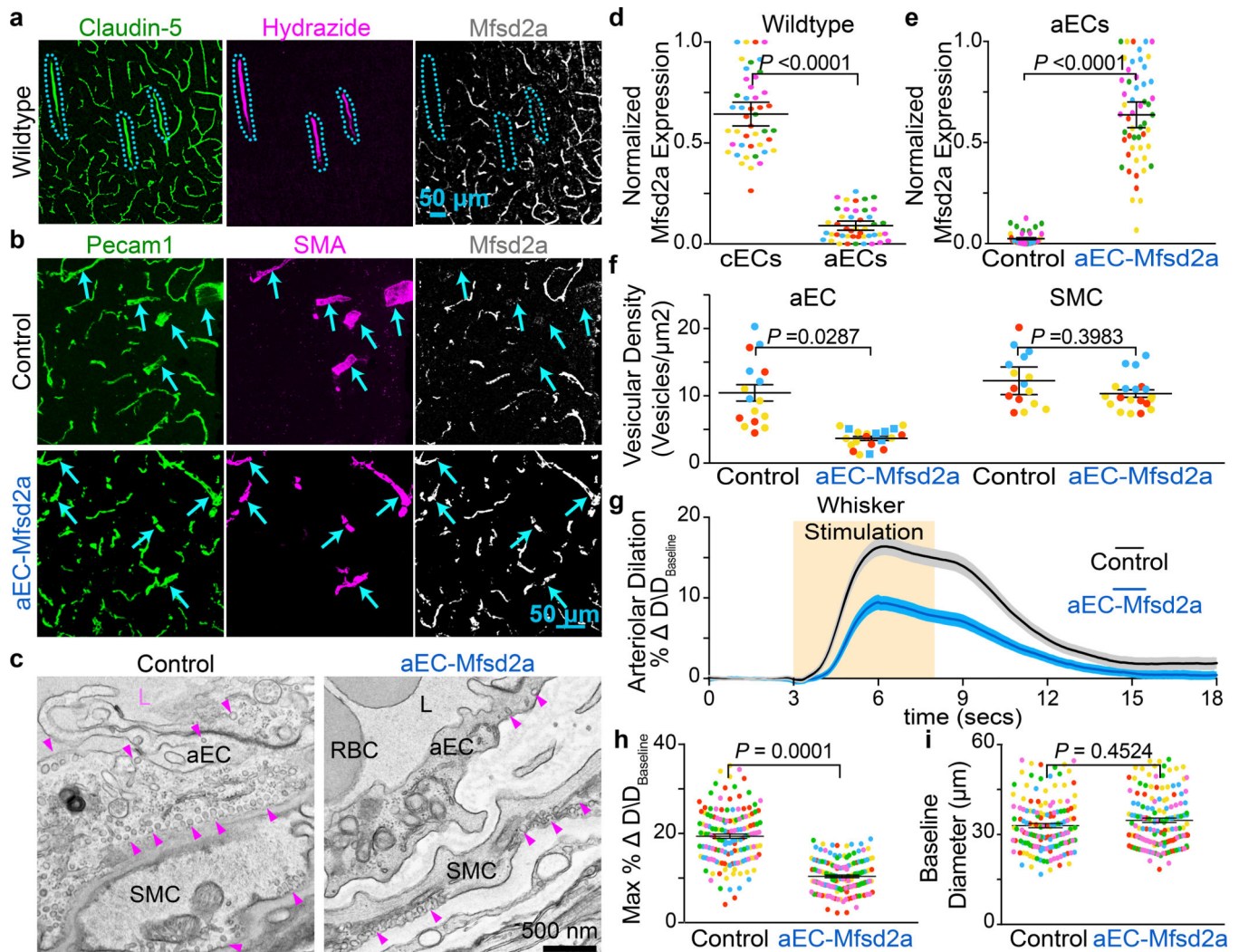(**c,d**). Data shown as mean ± s.e.m.

Fig 4. CNS arterioles lack Mfsd2a expression and ectopic expression of Mfsd2a in aECs downregulates caveolae and attenuates neurovascular coupling.

a, Immunostaining for Claudin-5, Hydrazide, and Mfsd2a on wild type adult brain sections demonstrates that Mfsd2a is not detectable in CNS arterioles. Blue hashes outline the Hydrazide+ arterioles. **b,** Immunostaining on adult brain sections for Pecam1, SMA, and Mfsd2a from control ($BMX:^{CreER-}$; $R26:^{LSL-Mfsd2a/+}$) and aEC-specific Mfsd2a overexpression mice ($BMX:^{CreER+}$; $R26:^{LSL-Mfsd2a/+}$). Arrowsheads point to SMA+ arteries. **d,** Quantification of the normalized immunofluorescence of Mfsd2a in cECs (Hydrazide-, Claudin-5+) and aECs (Hydrazide+, Claudin-5+) (n= 5 mice, 45 images) as shown in (**a**). **e,** Quantification of normalized immunofluorescence of Mfsd2a in aECs from control (n= 4 mice, 40 images) and aEC-specific Mfsd2a overexpression mice (n=5 mice, 51 images) as shown in (**b**). **c,f,** EM images of CNS aECs and SMCs (**c**) and quantification of the mean vesicular density (**f**) in aECs and SMCs from control (n= 3 mice, 20 arterioles) and aEC-specific Mfsd2a overexpression mice (n=3 mice, 22 arterioles). L, Lumen. SMC, smooth muscle cell, arrowheads point to caveolae. **g,h,i,** Time-course of change in arteriolar dilation (**g**) and max % change in arteriolar dilation (**h**) and baseline diameter (**i**) in control (n= 7

mice, 260 arterioles) and aEC-specific Mfsd2a overexpression mice (n= 5 mice, 193 arterioles. Statistical significance was determined by nested, unpaired, two-tailed t-test for (**d,e,f,h,i**). Data shown as mean ± s.e.m.